ACCSCIENCE PUBLISHING

International Journal of Bioprinting

RESEARCH ARTICLE

# Mixed ultrashort peptide bioinks for improved 3D bioprinting of self-healing trachea-like constructs

**Alexander U. Valle-Pérez[1,2‡], Dana Alhattab[1,3], Rui Ge[1,2], Eter Othman[1], Panayiotis Bilalis[1], Abdulelah Alrashoudi[1], Antonio Cárdenas-Calvario[1], Alan Eduardo Avila Ramírez[1], Zainab N. Khan[1], Manola Moretti[1,2], Christian Baumgartner[4], and Charlotte A. E. Hauser[1,2,4*]**

[1]Laboratory for Nanomedicine, Division of Biological and Environmental Science and Engineering, King Abdullah University of Science and Technology, Thuwal, Makkah Province, Saudi Arabia

[2]Computational Bioscience Research Center, Computer, Electrical and Mathematical Sciences and Engineering Division, King Abdullah University of Science and Technology, Thuwal, Makkah Province, Saudi Arabia

[3]Bio-ontology research group, Computer, Electrical and Mathematical Sciences and Engineering Division, King Abdullah University of Science and Technology, Thuwal, Makkah Province, Saudi Arabia

[4]Institute of Health Care Engineering with European Testing Center of Medical Devices, Faculty of Computer Science and Biomedical Engineering, Graz University of Technology, Graz, Styria, Austria

‡Current author affiliation: Marine Biology Research Division, Scripps Institution of Oceanography, University of California San Diego, San Diego, California, United States

***Corresponding author:**
Charlotte A. E. Hauser
(charlotte.hauser-funke@tugraz.at)

**Citation:** Valle-Pérez AU, Alhattab D, Ge R, *et al*. Mixed ultrashort peptide bioinks for improved 3D bioprinting of self-healing trachea-like constructs. *Int J Bioprint*. 2025;11(6):472-498. doi: 10.36922/IJB025320317

**Received:** August 7, 2025
**Revised:** September 16, 2025
**Accepted:** September 24, 2025
**Published online:** September 26, 2025



## Abstract

Concerns related to the trachea frequently arise from obstructive conditions and occlusions, such as tracheal stenosis, tracheomalacia, traumatic disruptions, and papillary thyroid carcinoma. These medical challenges underscore the need for new biomaterials to support tissue engineering for tissue regeneration. The advent of three-dimensional (3D) bioprinting technology has emerged as a pivotal advancement, facilitating the fabrication of patient-specific, biocompatible, cell-laden constructs. This technological advancement enables the controlled promotion of cell growth and tissue development, thereby offering a promising avenue for tissue regeneration. In this study, we developed mixed ultrashort peptide bioinks for the 3D bioprinting of a trachea-like construct that exhibits self-healing and elastic properties. We employed a stiffness prediction map (SPM) as an empirical tool to predict the physical characteristics and stiffness behavior of the mixed bioinks, thereby facilitating the optimization of the 3D bioprinting process. The SPM enabled the fine-tuning of these bioinks by identifying peptide mixtures that successfully mimic the natural stiffness of the perichondral niche microenvironment. These mixed bioinks successfully promoted mesenchymal stromal cell differentiation towards chondrocyte formation, thereby facilitating the biofabrication of elastic 3D-printed structures for trachea regeneration. Our bioinks exhibited remarkable printing resolution and mechanical properties while supporting cell growth and chondrogenesis. The bioprinted trachea-like model, cultured for up to 100 days, showed excellent mechanical properties, resulting a stable elastic biomaterial. This

study is the first to combine SPM with 3D bioprinting for the fabrication of a trachea-like model, supporting the development of advanced self-healing biomaterials for trachea tissue regeneration.

***Keywords*:** 3D bioprinting; Chondrocytes; Mesenchymal stromal cells; Self-healing biomaterials; Stiffness prediction map; Trachea-like model; Ultrashort peptide bioinks

## 1. Introduction

Advances in the development of biomaterials are desired to improve the reconstruction of physiologically relevant tissues and cellular grafts for tissue engineering and healthcare purposes.[1–3] The optimal biomaterials are biomimetic and can be used as models to simulate human tissue behavior, study cell growth and differentiation, investigate diseases, and potentially generate patient-specific non-immunogenic tissues for personalized medicine approaches. They also offer an alternative to *in vivo* animal models deployed in various tests, such as in drug screening assays.[4–8]

Three-dimensional (3D) bioprinting is an evolving technology that can be used to produce biomaterials replicating functional and biomimetic tissues and cellular grafts, advancing biomedical applications and healthcare. The technology has the potential to overcome donor shortages.[9] Conventional 3D printing falls into three main strategies: material extrusion, jetting, and vat polymerization.[10] On the other hand, 3D bioprinting technologies include cellular systems and are classified into nine main approaches: fused deposition modeling, stereolithography, inkjet, extrusion-based, laser-assisted, vat polymerization, magnetic, acoustic, and bioplotting.[10] Examples of 3D bioprinted constructs include organoids, human-scale mandible bone, ear-shaped cartilage, skeletal muscle, bone tissue, blood vessels, implanted vascular grafts, nose structures, trachea-like constructs, skin tissues, mouse brain structures, and full-size models of the human heart.[1,3,4,11–19]

In recent years, the use of computer-driven methods in bioprinting has led to significant progress.[9] Examples are the optimization of flow rates for peptide hydrogel-based 3D bioprinting, the integration of 3D bioprinting with multi-algorithm to identify microenvironment characteristics, the improvement of bioink formulation, and the tracking and classification of bioprinted organoids.[20–23] In addition, statistical procedures, such as response surface methodology (RSM), have been employed to optimize printing parameters in the bioprinting process. Applying RSM enables the construction of a dynamic printability window, which has recently been used for preparing polysaccharide-blended inks, optimizing printing speed and pressure conditions for silk–fibroin–gelatin-based constructs, developing *in situ* printability maps, and, more recently, statistically optimizing cell–hydrogel interactions in the area of green microbiology.[24–27]

Bioinks can be of natural or synthetic origin, which in turn determines the scaffold's biocompatibility, printability, and viscoelastic properties.[28,29] Natural-based bioinks include collagen, gelatin, chitosan, fibrin, silk, and alginate, while synthetic bioinks include polyethylene glycol (PEG), poly-N,N-dimethyl acrylamide (PDMA), acrylonitrile butadiene styrene, polylactic acid, polyvinyl alcohol (PVA), polyvinylpyrrolidone, polylactic-co-glycolic acid, and polycaprolactone (PCL).[10,30] Bioinks can also be mixtures of synthetic or natural and synthetic materials, resulting in the formation of multi-component hybrid bioinks, such as PLA–hydroxyapatite, PCL–alginate, PEG–gelatin, PCL–PEG, methacrylated hyaluronic acid–gelatin methacryloyl (GelMA), nanohydroxyapatite–PEG methacrylate, and PEG diacrylate–alginate, which could enhance biocompatibility and mechanical properties while affecting bioink printability.[30–33]

Peptide-based hydrogels are another class of promising bioinks for bioprinting due to their facile design, offering highly biocompatible and mechanically stable bioinks suitable as cellular scaffolds with a broad range of viscoelastic properties.[34] Peptide bioinks possess distinctive properties that integrate both natural and synthetic characteristics, rendering them particularly advantageous when compared with the other mentioned bioinks. Rationally designed ultrashort peptide compounds consisting of 3–7, preferably non-aromatic, amino acids are of particular interest due to their short sequence.[34,35] Through self-assembly, they form nano-fibrous networks and scaffolds, in the form of hydrogels, in aqueous solutions.[35,36] These thoroughly characterized self-assembling peptides exhibit a characteristic amphiphilic motif—consisting of a long hydrophobic tail of hydrophobic amino acids—and a short hydrophilic head group—mostly comprising a single hydrophilic amino acid. The peptide hydrogels' tunability makes them suitable

for 3D cell culture and tissue engineering, as they can span a broad range of viscoelastic properties, including hydrogel scaffold stiffness or softness, which in turn directly affects the material's storage and loss modulus, stress relaxation, and resistance to deformation under stress.[34] Previous studies have shown that peptide compounds containing lysine as a hydrophilic head group are excellent peptide bioinks, demonstrating the immediate solidification of cell-laden constructs under physiological salt conditions using extrusion-based 3D bioprinting, avoiding harsh situations such as UV exposure, reactive chemical additives, and elevated temperature conditions.[15,16,37]

Peptide hydrogels can also be used as biocontainment systems for clinical applications.[38] Peptide bioinks have been utilized in diverse applications, including 3D bioprinting of spheroids with induced pluripotent stem cells, printing brain models to study Parkinson's disease, modeling tissue to study leukemia, investigating colorectal cancer organoid development, printing ear models, and bioprinting large-scale constructs, as well as developing gel electrolytes, instant glues and hydrogel-based adhesives for environmental and biomedical applications.[12,15,16,39–46] This versatility has fueled growing interest in the use of multi-component bioinks for 3D bioprinting. Such bioinks can be formulated as mixtures from different ultrashort-peptide bioinks, forming peptide hybrid bioinks. For example, when combining the properties of various peptide bioinks that have different functional moieties, a previous study has formulated optimized mixed peptide bioinks as biofunctionalized peptide scaffolds to fabricate bioprinted colorectal organoids.[47]

Despite the progress made in bioprinting, several challenges still need to be addressed to produce fully functional tissues and cellular grafts.[48,49] These challenges include optimizing bioinks to promote more sophisticated bioprinting strategies without compromising cellular viability, ensuring the biocompatibility and structural stability of biomaterials, and better addressing biomimicry and functionality. Additionally, integrating vascularization into bioprinted structures, ensuring scalability, and replicating the complexity of organ architecture in bioprinted structures remain significant challenges.[14,48] More recently, there has been a growing interest in the 3D printing of smart and intelligent biomaterials, capable of reacting to both external and intrinsic stimuli for sustainability and healthcare applications.[50] Bioinks play a crucial role in forming the 3D structure with living cells, which can produce their own extracellular matrix (ECM) components during growth and development. To advance 3D bioprinted cellular grafts for further cell development, it is essential to establish a bioprinting strategy that combines all important factors, such as bioink materials, cellular components, and an optimal bioprinting strategy. Therefore, ongoing research is focusing on advanced bioprinting processes using optimized biomaterials with scalable, functional, biocompatible, and biomimetic characteristics to mimic tissues and cellular grafts.

There is a need to develop alternative tracheal replacements using tissue engineering technologies to advance the treatment and rehabilitation of patients with tracheal pathology.[51] Therefore, 3D printing and bioprinting technologies have been applied to engineer materials (e.g., polymers of synthetic origin) and biomaterials (e.g., biomimetic and biocompatible living materials) for tracheal tissue engineering, such as constructing artificial organs for the trachea. Although synthetic materials may exhibit strong structural robustness, they often have lower cell biocompatibility and a higher chance of inducing immune rejection. Conversely, biomaterials may exhibit high biocompatibility and low immune response, but have insufficient mechanical properties.

Remarkable progress has been made in the 3D printing of trachea-like constructs. For example, the 3D bioprinting of trachea-mimetic cellular construct with clinically relevant size has been performed through a two-step printing strategy and a bioink that consists of PCL-based thermoplastic polymer; the long segmental tracheal replacement has been conducted using PCL and collagen bioink mixture; the development of biomimetic trachea through a modular ring strategy with poly(sebacoyl diglyceride) and PCL bioink mixture; the dual-nozzle extrusion bioprinting of cartilage-vascularized fibrous tissue-integrated trachea with photo-cross-linkable GelMA and chondroitin sulfate methacrylate bioink mixtures; and the bioprinting of patient-matched trachea with PCL and HyStem®-HP hydrogel bioinks hydrogel bioinks.[13,52–55] Alternative non-printing strategies include the use of fully synthetic polymers and the bioengineering of tracheal prostheses with autologous chondrocytes and decellularized trachea scaffolds.[56,57] Nevertheless, there are still bottlenecks that limit the translation of bioengineered tracheostomies for medical applications. These limitations include insufficient material mechanics (e.g., material weakening over time and longitudinal rigidity), lack of biomimetic properties (e.g., low cell density, mucous accumulation, and lack of epithelial lining), adverse immune response (e.g., inflammation and fibrosis), biomaterial infection (e.g., contamination during cultivation), and low functionality (e.g., uniform geometries and transmural pressures).[58–62]

This study employed the stiffness prediction map (SPM) to formulate mixed ultrashort peptide bioinks for extrusion-based robotic 3D bioprinting. The approach

allows the selection of peptide scaffolds with initial stiffness supportive of stromal cell differentiation into chondrocytes, enabling the development of customizable bioinks suitable for 3D bioprinting. SPM enhanced the ability to assess the rheological properties of mixed ultrashort peptide hydrogels, allowing robust evaluation of materials' stiffness and accelerating mesenchymal stromal cell (MSC) differentiation into chondrocytes. Through SPM, we identified and developed three mixed ultrashort-peptide bioinks that, in addition to being highly biocompatible, exhibited diverging viscoelastic properties compared to bioinks made from single peptides. Additionally, the mixed bioinks promoted the formation of chondrogenic cell nodules in 3D bioprinted constructs cultured for 28 days, as evidenced by changes in gene expression and morphology. Based on these results, we selected the optimal-performing bioink in terms of printability and cell-scaffold interaction to bioprint a trachea-like model. The resulting construct exhibited accelerated self-healing (due to the presence of cells and their subsequent enrichment of the hydrogel scaffold with ECM components), structural stability, and remarkable elastic properties, highlighting it as a promising self-healing biomaterial for tracheal tissue regeneration. This study introduced a statistical cutting-edge approach to optimizing mixed peptide bioinks for 3D bioprinting, enabling automated production of stable and self-healing cellular constructs for long-term culture.

## 2. Materials and methods

### 2.1. Peptide synthesis

N- and C-terminus protected peptides Ac–Ile–Ile–Cha–Lys–$NH_2$ (IIZK) and Ac–Ile–Ile–Phe–Lys–$NH_2$ (IIFK) were synthesized through solid-phase peptide synthesis using a CS136X synthesizer (CSBio, USA). After synthesis, the peptides were removed from the resin using a mixture of 95% trifluoroacetic acid, 2.5% tri-isopropyl silane, and 2.5% water at room temperature for 2 h. The peptide was then precipitated by adding cold diethyl ether to the peptide solution and kept overnight at 4°C. The precipitated peptide was separated from the supernatant by centrifugation at 5000 rpm for 5 min using Eppendorf 5810R (Eppendorf, Germany). Finally, the peptide was purified using reverse-phase high-performance liquid chromatography with a C-18 column (2–98% acetonitrile in 15 min) at a flow rate of 20 mL/min and collected at a yield of over 60%.

### 2.2. G-code design and slicing

The 3D models were configured with computer-aided design in SolidWorks® version 2024 (Dassault Systèmes, USA), optimized with Slic3r version 1.3.0 (https://slic3r.org/), and translated into G-codes using the Repetier-Host software 2.3.2 (Hot-World GmbH & Co. KG, Germany).

### 2.3. Cell culture

Human bone marrow MSCs were cultured with Minimum Essential Medium (MEM)-α and supplemented with 10% mesenchymal stem cells (MSC-qualified) fetal bovine serum (FBS), 1% penicillin/streptomycin, and 1% GlutaMAX (Thermo Fisher Scientific, USA). The cells were thawed, cultured, and subsequently incubated at 37°C with 5% $CO_2$, and were sub-cultured when reaching 95% confluency using 0.25% trypsin.

### 2.4. Bioink preparation

Peptide powders were weighed at different peptide ratios (see Table 1) with a Mettler Toledo analytical balance (XPR204DUE, Switzerland). Initially, the measured first peptide type was added to a 2 mL glass vial, followed by the addition of the second peptide type to the same vial. The glass vial was sealed with a cap, and the mixed peptide powder was gently vortexed for 30 s. A class II biological safety cabinet was sterilized by decontaminating surrounding surfaces with 70% ethanol and UV irradiation for 30 min to ensure sterile working conditions. Subsequently, the mixed peptide-powder-containing glass vial cap was removed in the biosafety cabinet, and the UV light was applied for 1 h to prevent external contamination. Then, 900 µL of Gibco™ cell culture grade distilled water (Thermo Fisher Scientific, USA) was added to the vial, and the mixture was vortexed for 30 s to obtain a homogeneous solution, followed by sonication for 15 min to remove air bubbles. The resulting bioinks were used for subsequent 3D bioprinting experiments.

### 2.5. 3D bioprinting

Bioprinting experiments were conducted using a robotic 3D bioprinter (Dobot Magician, Dobot, China) composed of a four-degrees-of-freedom robotic arm, a custom-designed dual-coaxial nozzle, microfluidic pumps, and a stirring hot plate (RCT basic, IKA, Germany). The robotic arm was interfaced with Repetier-Host. The printing files were designed using SolidWorks and sliced into G-code through the Slic3r and Repetier-Host software. The used dual-coaxial nozzle was fabricated according to the literature.[12] The commercial microfluidic pumps were controlled simultaneously using the automated pulse mode with square waves.[63] According to the viscosity and surface tension results, flow rates were identified to extrude the formulated mixed ultrashortpeptide bioinks with minimal clogging and clumping during the extrusion-based bioprinting process. The optimized pumping flows were 40–45 µL/min (peptide solution), 15–20 µL/min (5× phosphate-buffered saline [PBS]), and 15 µL/min (1× PBS with cells) for each of the pumps, respectively. It is essential to highlight that the interaction between PBS and peptide solution within the nozzle forms the gel

**Table 1. State-of-the-art peptide-based trachea engineering and bioinks formulation**

| Peptide-based trachea-like construct | Mixed peptide bioink | Ratio | Concentration (mg/mL) | | | Molarity (mM) | | | Reference |
|---|---|---|---|---|---|---|---|---|---|
| | | | IIZK | IIFK | IZZK | IIZK | IIFK | IZZK | |
| Extrusion-based bioprinting of a 3.0-cm-high, 2.2-cm-diameter, self-healing, elastic human trachea-like model that is cultured for up to 100 days with hBM-MSCs and MSC-derived chondrocytes. The 3D-printed structures exhibit excellent printability, high resolution, low clogging, and strong structural rigidity. | Bioink 1 | 3:1 | 7.1 | 2.4 | – | 12.5 | 4.3 | – | This work |
| Extrusion-based bioprinting of a 1.36-cm-high, self-healing, small-diameter trachea-like model that is cultured for up to 28 days with hBM-MSCs and MSC-derived chondrocytes. The 3D-printed structures exhibit excellent printability, high resolution, low clogging, and strong structural rigidity. | Bioink 2 | 1:1 | 4.1 | 4.1 | – | 7.2 | 7.2 | – | This work |
| Extrusion-based bioprinting of a 1.39-cm-high, self-healing, small-diameter trachea-like model that is cultured for up to 28 days with hBM-MSCs and MSC-derived chondrocytes. The 3D-printed structures exhibit excellent printability, high resolution, and minimal clogging, but with reduced structural stability. | Bioink 3 | 1:3 | 2.4 | 7.1 | – | 4.2 | 12.6 | – | This work |
| Extrusion-based bioprinting of 1-cm-high, small-diameter cylinders that are cultured for up to 24 and 30 days with HDFn and hBM-MSC cells, respectively. The 3D-printed constructs exhibit sagging issues, resulting in low printability. | Single peptide IIFK | – | 13.0 | – | – | 23.5 | – | – | [12] |
| Extrusion-based bioprinting of 3.8-cm-high, small-diameter cylinders that are cultured for up to 24 and 30 days with HDFn and hBM-MSCs, respectively. The 3D-printed constructs exhibit superb printability, although potential clogging issues arose due to bioink overgelation. | Single peptide IIZK | – | – | 13.0 | – | – | 23.1 | – | [12] |
| Extrusion-based bioprinting of a 4-cm-high, small-diameter cylinder that is cultured for up to 30 days with hBM-MSC-derived chondrocytes. The 3D-printed constructs exhibit superb printability, although potential clogging issues arose due to bioink overgelation. | Single peptide IZZK | – | – | – | 13.0 | – | – | 22.88 | [12] |
| Extrusion-based bioprinting of a 1-cm-high, 1-cm-diameter cylinder that was cultured for up to 14 days with hBM-MSCs and MSC-derived chondrocytes. The 3D-printed constructs exhibit superb printability, although potential clogging issues arose due to bioink overgelation. | Single peptide IIZK | – | 13.0 | – | – | – | 23.1 | – | [73] |
| Extrusion-based bioprinting of a 3.8-cm-high, small-diameter cylinder that was cultured for up to 14 days with hBM-MSCs and MSC-derived chondrocytes. The 3D-printed constructs exhibit superb printability, although potential clogging issues arose due to bioink overgelation. | Single peptide IZZK | – | – | – | 13.0 | – | – | 22.88 | [73] |

Abbreviations: hBM-MSC, human bone marrow-derived mesenchymal stromal cell; HDFn, human dermal fibroblast cells.

material for extrusion-based bioprinting. The cells were concentrated in 500 µL of FBS, MSC-qualified, and slowly pushed throughout the tubbing. Transparent square cover slides were thoroughly washed in 70% ethanol and left under UV irradiation for 30 min. The bioprinting process was performed inside a class II biological safety cabinet. Tweezers were sterilized using MLS-3781L autoclave (Panasonic, Japan) at 121°C for 15 min.

### 2.6. Printability and shape fidelity assessment

The mixed ultrashort peptide bioinks were 3D-printed into trachea-like structures. The ImageJ software version 1.54p (https://imagej.net/ij/) was used to calculate the width and height of the samples. Photographs were taken from the

side and from the top, with a calibration ruler included in the frame to calibrate pixel dimensions against actual measurements.

### 2.7. Chondrogenic differentiation

Bioprinted constructs were incubated at 37°C, supplemented with 5% $CO_2$ and MEM-α for 7 days. Afterward, chondrogenic media (PT-3925) and tumor growth factor (TGF)-β3 (PT-4121) were mixed and added (until completely covering the structures), and the cultures were maintained for 28 days with medium exchanged every 2 days. The chondrogenic media consisted of 1 mL dextrose (PT-4130G), 2 mL ascorbate (PT-4131G), 2 mL insulin–transferrin–selenium with supplements (PT-4113G), 2 mL pyruvate (PT-4114G), 2 mL proline (PT-4115G), 200 µL gentamicin sulfate–amphotericin (GA-1000; PT-4505G), and 4 mL *L*-glutamine (PT-4140G). The lyophilized TGF-β3 was prepared by adding 200 µL of sterile 4 mM hydrochloric acid (supplemented with 1 mg/mL bovine serum albumin) to 2 µg TGF-β3, and aliquots were stored at −80°C. All of these reagents and media were purchased from Lonza (Switzerland).

### 2.8. RNA extraction and quantification

Total RNA was extracted using Trizol (15596026, Thermo Fisher Scientific, USA) and Qiagen RNeasy Mini kit (74104, Qiagen, USA). The 3D bioprinted samples were digested by adding 2 mL of TRIzol reagent, mixed through pipetting, and stored at −80°C until further processing. The samples were dissolved at room temperature for 5 min, and 200 µL of chloroform per mL of TRIzol was added to each sample. They were vortexed for 20 s and centrifuged (Centrifuge 5424 R, Eppendorf, Germany) at 10,000 g for 18 min at 4°C. The aqueous phase was carefully removed and transferred to sterile RNAse-free microtubes, and an equal amount of RNA-free EtOH was added. The samples were inverted three times, loaded into the RNeasy columns, and centrifuged for 30 s at 8000 g. The flow-through was discarded. Then, 700 µL of RW1 buffer was added to the columns and centrifuged for 30 s at 8000 g. The columns were transferred to new collection tubes, and 500 µL of RPE buffer was added. The samples were centrifuged for 30 s at 8000 g. Again, 500 µL of RPE buffer was added, and samples were centrifuged for 2 min at 8000 g. The flow-through was discarded. The columns were centrifuged for 1 min at 8000 g. Columns were transferred to new collection tubes, and 35 µL of RNase-free water was added directly to the membrane. Samples were left at room temperature for 1–2 min and then centrifuged at 8000 g to elute the RNA. The RNA samples were quantified by measuring 2 µL from each sample using the Nanodrop 2000 spectrophotometer instrument (Thermo Fisher Scientific, USA) and were immediately stored at −80°C. The RNaseZap cleaner (AM9780, Invitrogen, USA) was used during the entire experiment.

### 2.9. Complementary DNA synthesis

The RNA was reverse-transcribed into complementary DNA (cDNA). First, the extracted RNA samples were normalized (**Equation I**). Subsequently, the SuperScript™ VILO™ Master Mix (11755-050, Thermo Fisher Scientific, USA) was used for cDNA synthesis. A 20 µL total reaction volume was prepared by adding 4 µL Master Mix and 5µL normalized RNA, then filling to 20 µL with nuclease-free water. The samples were placed in a thermomixer (Eppendorf ThermoMixer® C, Germany) with incubation cycles: 25°C for 10 min, 42°C for 90 min, and 85°C for 5 min. The cDNA was diluted at a 1:5 ratio by mixing 20 µL of cDNA with 80 µL of nuclease-free water. Aliquots were stored at −20°C.

$$Normalized\ RNA\ volume = \frac{800\ ng}{Extracted\ RNA\ in\ ng\ per\ \mu L} \quad \text{(I)}$$

### 2.10. Quantitative polymerase chain reaction for gene expression analysis

The quantitative polymerase chain reaction (qPCR) was performed using the TaqMan gene expression assay (Table 2) and TaqMan Fast Advanced master mix (4444557, Thermo Fisher Scientific, USA). Briefly, a total volume of 150 µL solution, composed of 100 µL master mix, 10 µL TaqMan probe, and 40 µL nuclease-free water, was added to each well and mixed. Subsequently, 2.5 µL of the diluted cDNA was added per well. The reverse transcription-qPCR was performed using the QuantStudio 3, 0.1 mL instrument (Thermo Fisher Scientific, USA) with thermal cycling parameters: 50°C for 2 min, 95°C for 2 min, and 40 cycles of 95°C for 1 s and 60°C for 20 s.

### 2.11. Viscoelastic characterization

The viscoelastic properties of the peptide hydrogels, including mechanical stiffness, viscosity, and thixotropy, were analyzed using the Ares-G2 Rheometer (TA Instruments, USA) equipped with an advanced Peltier system (APS). The stiffness of the peptide hydrogels was measured using an 8-mm parallel plate with a gap of 1.5 mm between plates. The peptide concentrations were prepared according to the SPM's experimental design. The peptide hydrogel concentrations were prepared by mixing 135 µL of peptide solution with 15 µL of PBS in a 9-mm internal diameter Sigmacote-coated glass ring. The rings were kept overnight inside Petri dishes at room temperature,

**Table 2. TaqMan probes for gene expression**

| Gene | Catalog number of TaqMan probe | Catalog number |
|---|---|---|
| Collagen I (*COLI*) | Hs00164004_m1 | 4331182 |
| Collagen II (*COLII*) | Hs00264051_m1 | 4331182 |
| Collagen X (*COLX*) | Hs00166657_m1 | 4331182 |
| Aggrecan (*ACAN*) | Hs00202971_m1 | 4331182 |
| *SOX9* | Hs00165814_m1 | 4331182 |
| *SOX5* | Hs00374709_m1 | 4331182 |
| *RUNX2* | Hs01047973_m1 | 4331182 |
| *ALPL* | Hs01029144_m1 | 4331182 |
| *CEBPB* | Hs00942496_s1 | 4331182 |
| *PPARG* | Hs01115513_m1 | 4331182 |
| *GAPDH* | Hs99999905_m1 | 4448490 |

surrounded by water and tightly sealed to avoid dehydration. The viscoelastic properties were analyzed through three successive tests: time-sweep, frequency-sweep, and amplitude-sweep. The time-sweep test was first performed for 5 min with an angular frequency and a strain of 1 rad/s and 0.1%, respectively. The frequency-sweep test was subsequently performed on the sample with a range of angular frequency of 0.1–100 rad/s and the same strain of 0.1%. The amplitude-sweep test was performed by applying a gradual strain increase from 0.01 to 100% at 1 rad/s angular frequency. The interpolation from the oscillation strain curves was performed using the trace interpolation tool in the OriginPro software (OriginLab, USA). The thixotropic properties of the mixed ultrashort-peptide bioinks were measured using an angular frequency of 1 rad/s and a sampling rate of 1 pts/s. An initial strain of 0.1% was applied to the peptide hydrogel for 5 min. Then, the peptide hydrogel was exposed to different strains ranging from 100% (1 min) to 0.1% (10 min) with 11 oscillation cycles. The total duration of the thixotropy test for each sample was 3600 s.

### 2.12. Measurement of self-healing properties

The self-healing capabilities of the 3D bioprinted structures were analyzed using the Ares-G2 Rheometer equipped with APS and an 8 mm parallel plate. The 3Dbioprinted structures were placed on top of the parallel plate, and the self-healing properties of the mixed ultrashort peptide bioinks were measured with an angular frequency of 1 rad/s and a sampling rate of 1 pts/s. An initial strain of 0.1% was applied to the peptide hydrogel for 5 min. Then, the peptide hydrogel was exposed to different strains ranging from 100% (1 min) to 0.1% (10 min) with 11 oscillation cycles. The total duration of the thixotropy test for each sample was 3600 s.

### 2.13. Design of experiments and response surface methodology

The Minitab version 21.4.1 software (Minitab, USA) was used to derive an initial model representation for the interaction between the IIZK and IIFK peptides and their measured responses regarding stiffness. First, experiments were designed according to the RSM. A central composite design for two continuous factors (IIZK and IIFK) was selected here. The design consisted of one center point, four cube points, and four axial points, resulting in a total of nine points to build the matrix using a face-centered design with an α of 1 (Figure S1). The design levels considered the lowest and highest values of 2 and 8 mg/mL, respectively. This concentration range was selected based on the printability window for extrusion-based bioprinting with the IIZK and IIFK bioinks reported in previous studies to prevent clogging during the bioprinting process.[12] The performance of four RSM models was evaluated, considering their $R^2$, adjusted $R^2$, predicted $R^2$, and standard deviation to select the optimal mathematical model for fitting the data (Tables S2 and S3; Figures S2–S5). The top-performing model was chosen for fitting the experimental data; the design of experiments (DOE) and analysis of variance (ANOVA) from the top-performing model are shown in detail in Tables S4 and S5. For each of the nine mesh points according to the design matrix (Figure S1), 20 samples were prepared and measured ($n$=20), resulting in 188 experimental rheology measurements. The data distribution of the rheology measurements was visualized in Figure S6. Following experimental measurements, data preprocessing was carried out to identify potential outliers using boxplot visualization, corroborated by $Z$-score and mean absolute deviation (MAD) methodologies. The MAD threshold values for outlier detection were calculated (Table S6) according to Equations II and III.[64]

After identification, outliers were removed from the dataset and substituted with new measurements. Subsequently, the processed dataset was fed into Minitab to derive an RSM-based mathematical modeling equation that represents the proposed 3D representation of the DOE (Equation IV) according to the experimental data and DOE from the top-performing model (Tables S2, S3, & S7). The data distribution, residuals, and adjustment to the modeling equations can be found in the supplementary information (Figures S2–S6; and Tables S2–S7). Further information on the RSM methodology can be found in the literature that applied RSM to model the mixing of different materials in the formulation of bioinks.[27,65,66] Lastly, the 3D representation of the SPM was plotted and visualized in MATLAB version R2024b (MathWorks, USA).

$$\textit{Outliers maximum threshold value} = \textit{median}\ (X) + (\alpha \times MAD) \quad \text{(II)}$$

$$\textit{Outliers maximum threshold value} = \textit{median}\ (X) + (\alpha \times MAD) \quad \text{(III)}$$

**where** $X$ was the $n$ original observations, set to 3 according to the literature.

$$\gamma = (\pm \delta_0) \pm \delta_1\alpha \pm \delta_2\beta \pm \delta_3\alpha^2 \pm \delta_4\beta^2 \pm \delta_5\ (\alpha \times \beta) + \varepsilon \quad \text{(IV)}$$

where $\gamma$ represents the storage modulus (response in Pa), $\delta$ (0–5) represents the obtained constants from the statistical equation from the fit of the experimental data, α represents peptide 1 (factor 1 in mg/mL), $\beta$ represents peptide 2 (factor 2 in mg/mL), and ε represents the total error from the model

### 2.14. Measurements of the bioinks' viscoelastic properties

The viscoelastic properties of the bioinks were analyzed using the Ares-G2 Rheometer equipped with APS. Viscosity measurements were conducted at 25°C using a 25 mm parallel plate geometry and a 0.5 mm gap between plates. The bioinks were prepared by mixing IIZK and IIFK at a 1:1, 1:3, or 3:1 ratio to a final concentration of 10 mg/mL. Viscosity was assessed in both solution and gel states. For gel measurements, 225 µL of bioink solution was placed on the Peltier plate, followed by the addition of 25 µL 10× PBS, and allowed to react for 10 min before performing a shear rate sweep (0.01–50/s). For solution measurements, 250 µL of bioink solution was placed on the Peltier plate and directly measured.

### 2.15. Gelation tests

Gelation tests were performed following established protocols for peptide hydrogel formation.[12] Peptide powder was dissolved in 900 µL of Mili-Q water and vortexed until fully dissolved, and solubility was recorded. To induce gelation, 100 µL of 10× PBS (without $Ca^{2+}$ and $Mg^{2+}$) was added to the solution. The vial was left at room temperature, and gel formation was monitored visually to determine gelation time.

### 2.16. Thermomechanical characterization

Thermogravimetric analysis (TGA) was performed on dried samples (10 mg initial weight) using a TGA 5500 (TA Instruments, USA). Samples were heated in platinum pans from 25 to 700°C at 10°C/min under a $N_2$ atmosphere. Weight loss curves were plotted, and first derivatives were calculated. Subsequently, differential data were smoothed using the Savitzky–Golay method. All data plotting, derivative calculations, and signal processing were performed in the OriginPro 2022b software.

### 2.17. Measurement of surface tension

A force tensiometer (Kruss K100 MK2, KRÜSS GmbH, Germany) was used to measure the surface and interfacial tension of samples. A custom glass probe was prepared by cutting the glass to the desired size of 15×25×1 mm. The tensiometer was stabilized at room temperature prior to use. For each measurement, 3 mL of peptide solution (10 mg/mL) was placed in a 10 mL beaker, and the probe was gently placed on the surface of the liquid. Detection parameters were set to a speed of 10 mm/min, sensitivity of 0.005 g, and immersion depth of 1 mm.

### 2.18. Phase contrast and epifluorescence microscopy

Kinetic imaging experiments were performed using the DMI3000 B phase contrast microscope (Leica, Germany) on days 5, 10, 15, and 28. Photographs and videos of the full-sized trachea-like ring were recorded using the EVOS M7000 epifluorescence microscope (Invitrogen, USA).

### 2.19. Assessment of cell viability

The viability of the bioprinted trachea-like structures was assessed using the live/dead cell viability cytotoxicity kit (L3224, Thermo Fisher Scientific, USA). Calcein acetoxymethyl ester was used to detect live cells, while ethidium homodimer-I was used for dead cells. Media was discarded, and the structures were subsequently washed three times with 1× PBS. Staining solution, consisting of 3 µL calcein, 6 µL ethidium homodimer, and 3 mL 1× PBS, was prepared and added until the structure was submerged. The samples were covered with aluminum foil and left in an incubator for 1 h. After incubation, the staining solution was discarded, and 3 mL of 1× PBS was added. The entire procedure was carried out under dark conditions to avoid

photobleaching. The structure viability was assessed after 15, 24, and 100 days.

### 2.20. Cytoskeleton staining

Cells were previously fixed using methanol-free formaldehyde. The media were removed for fixation, and constructs were washed three times with 1× PBS. Then, 1 mL of 16% (w/v) formaldehyde solution was diluted with 3 mL of 1× PBS, resulting in 4% formaldehyde. The construct was incubated at room temperature for 1 h, followed by three washes with 1× PBS, then covered with parafilm, and stored at 4°C. Next, a blocking buffer—consisting of 1.25 mL FBS, 25 µL TWEEN 20, and 5 mg sodium azide—and a cytoskeletal buffer—composed of 125 µL Triton 100, 15.2 mg $MgCl_2$, and 2.6 g sucrose—were prepared and filled to 25 mL using 1× PBS. For staining, both solutions were placed on ice for 10 min. Construct media were removed, and cold cytoskeletal buffer was added and incubated for 5 min. Then, the construct was washed twice with 1× PBS. Subsequently, the blocking solution was added, and the sample was left incubating at room temperature for 1 h. The primary antibody solution, consisting of actin-phalloidin, was diluted by mixing 10 µL of the antibody in 4 mL of 1× PBS. Samples were immersed in the primary antibody solution and incubated for 1 h at room temperature while covered with aluminum foil. Then, the solution was removed, and the construct was washed with 1× PBS, followed by adding 4 µL of 4',6-diamidino-2-phenylindole (Thermo Fisher Scientific, USA) for every mL of the final volume, and then incubating for 5 min at room temperature with minimal light exposure.

### 2.21. Confocal imaging

The bioprinted constructs were imaged using a laser scanning confocal microscope (LSM 880 with Airyscan, ZEISS, Germany). Z-stack and 2D images were collected throughout the experiment using a pinhole size of 1.25 airy units. Images were postprocessed using the ZEN (black edition) software (ZEISS, Germany).

### 2.22. Scanning electron microscopy imaging of cell-laden bioprinted scaffolds

Peptide scaffolds were fixed with 25% electron microscopy-grade glutaraldehyde. The media was removed, and the construct was washed three times with 1× PBS. Then, 1 mL of 25% glutaraldehyde was diluted in 9 mL of 1× PBS to a final concentration of 2.5% glutaraldehyde solution. The solution was added to the sample and incubated in the fume hood for 1 h, followed by washing with 1× PBS. Then, 2 mL of 4% osmium tetroxide solution (Polysciences, USA) was mixed with 8 mL of 1× PBS to a final osmium tetroxide concentration of 1%. The diluted osmium solution was added to the structure and incubated for 1 h under dark conditions. Then, the osmium solution was discarded, and the samples were washed three times with $dH_2O$ for periods of 15 min each. Subsequently, the samples were dehydrated by gradually increasing ethanol concentrations (20, 40, 60, and 80% in 2 mL $dH_2O$ for 5 min periods each). The sample was finally dehydrated in 2 mL of 100% ethanol for 2 h. For 3D bioprinted samples, dehydrated gels were mounted on 12-mm-outer-diameter PELCO Tabs™ (Ted Pella, Inc., USA) and dried using the Critical Point Dryer CPD300 (Leica, Germany). Immediately after CPD drying, the samples were sputter-coated with a 5 nm Pt layer using the K575X Sputter Coater (Quorum Technologies, UK) under 20 mA for 40 s. Scanning electron microscopy (SEM) images were acquired using the Teneo SEM (FEI Company, USA) with an accelerating voltage of 3kV and a current of 13 pA for cell imaging.

### 2.23. Scanning electron microscopy imaging of peptide fibers

Peptide bioinks were prepared at a concentration of 10 mg/mL. Then, 9 µL of peptide solution was mixed with 1 µL of 10× PBS on a silicon wafer. The bioinks were left at room temperature for 2 h in sealed containers and subsequently dehydrated through an ethanol gradient (20, 40, 60, and 80%, 5 min each). The bioinks were finally left in a 100% ethanol solution for 2 h. Subsequently, the dehydrated bioinks were dried using the Automegasamdri-916B series C critical point dryer (Tousimis, USA). The samples were mounted on an SEM stub using silver paste and sputter-coated with a 5-nm-thick iridium layer. SEM images were acquired using the Teneo EM with an accelerating voltage of 5kV and a current of 50 pA.

### 2.24. Atomic force microscopy

Atomic force microscopy (AFM) topography data were collected on three mixtures of the peptides at IIZK-to-IIFK ratios of 3:1, 1:1, and 1:3, with final concentrations of 9.39, 8.12, and 9.39 mg/mL, respectively. The peptides were dissolved in Milli-Q water, and 10 µL of the solution was cast on a freshly cleaved mica sheet and dried immediately with an $N_2$ stream. The samples were immediately measured using a JPK Nanowizard III (Bruker, USA) and a calibrated AFM probe (AC240TS, Olympus, Japan) with a nominal resonance frequency of 65 kHz and a spring constant of 0.2 N/m. Several images were acquired through a scan size of 2×2 µm and a 1024×1024 lines per pixel resolution. The topography scans were then processed by applying a three-point surface flattening and assigning the lowest value to zero. A mask was applied to the fibers to isolate them for 1D height analysis.

### 2.25. Raman spectroscopy

Raman spectra were acquired using a confocal Raman spectrometer (WiTEC Alpha 300R, Oxford Instruments, UK) with a backscattering configuration, a laser wavelength

of 532 nm, and a power of 12 mW at the source. In this context, the mixed ultrashort peptide bioinks were prepared at the following IIZK-to-IIFK ratios: 3:1, 1:1, and 1:3, with a final concentration of 10 mg/mL. The peptide hydrogels were immediately measured under the micro-Raman spectrometer, acquiring several spectra at different locations for each sample, with an integration time of 3 s per 10 accumulations. The acquired spectra were then averaged, cropped to the Amide I range from 1500 to 1800 $cm^{-1}$, baseline subtracted by endpoints weighing, and fitted with the most intense peak by a Voigt function in the 1660–1678 $cm^{-1}$ range, which is specific for beta-sheet secondary structures. In this way, the fitting procedure was constrained to identify the Raman shift at which the strongest peak signal occurred.

### 2.26. Molecular dynamics simulations of peptide assembly

In this study, molecular dynamics (MD) simulations were employed to explore the self-assembly process of mixtures of IIZK and IIFK peptide molecules in an aqueous environment, focusing on fiber formation at the atomic level. Utilizing GROMACS 2018 (https://www.gromacs.org/index.html), the simulations leveraged the optimized potentials for liquid simulations force field to model interactions.[67,68] For the specific residue cyclohexylalanine (Z), we generated topology parameters using the LigParGen webserver (https://zarbi.chem.yale.edu/ligpargen/).[69] Water molecules were represented using the simple point charge extended model, and a 2-fs timestep was adopted for integrating motion equations. The simulations were configured with cubic boxes, applying periodic boundary conditions. The particle mesh Ewald method was used for long-range electrostatic interactions, while a cutoff of 1.4 nm was set for short-range non-bonded interactions.[70] The MD simulation process comprised three stages: energy minimization, equilibration, and production MD. Initially, energy minimization relaxed the peptide structures, ensuring a realistic starting point. Equilibration occurred in two phases, with the first phase number volume temperature (NVT ensemble) stabilizing temperature and the second number pressure temperature (NPT ensemble) stabilizing pressure. The production phase employed a Berendsen Barostat and a V-Rescale thermostat, maintaining a standard pressure of 100 kPa and temperature of 26.85°C over a total simulation duration of 100 ns (**Tables S8–S12**).[71,72] These simulations ran on 512 Intel Haswell cores (USA) at 2.3 GHz. For each peptide, three configurations were examined: assemblies of 4 or 5, 10, and 60 peptides. Peptides were evenly distributed within the simulation box, surrounded by water. More details regarding peptide concentration and number of peptides are reported in the Supplementary material (**Table S8**).

### 2.27. Statistical analysis

The TGA thermochemical characterization, viscosity, and surface tension results were performed in duplicate. 3D bioprinting experiments were performed in triplicate. The gene expression, thixotropic, and self-healing experiments were performed in duplicate. The rheological measurements for the SPM strategy consisted of 188 measurements. Subsequent statistical analyses for SPM (i.e., data distribution, experimental fitting and statistical modeling, DOE, ANOVA, residual plots, Pareto charts, and RSM) were performed using the Minitab software. For multiple comparisons, the Tukey test was used to determine the statistical significance of the population mean, with an alpha value of $p<0.05$, as determined by the OriginPro software (version 2024b). For outlier identification, the $Z$-score, MAD, and threshold limits were calculated as previously described in the DOE and RSM section. The derivative weight of the TGA data was calculated using the OriginPro software. Longitudinal and orthogonal profiles were applied for AFM image analysis. The dimensions of the 3D bioprinted trachea were analyzed using the ImageJ software. The SPM model was plotted and visualized using the MATLAB software.

## 3. Results and discussion

### 3.1. Stiffness prediction map for improved scaffold design of 3D bioprinted trachea-like constructs

To formulate mixed ultrashort peptide bioinks for 3D bioprinting of an elastic and self-healing trachea-like model, two ultrashort peptides, IIZK and IIFK, were selected due to their characteristic properties. We have previously reported on peptides IIZK and IIFK, demonstrating high mechanical strength with fast gelation kinetics for IIZK and a three-fold lower mechanical strength with slower gelation kinetics for IIFK, thereby rendering them suitable for stem cell growth and proliferation.[12] In that study, both peptides were used at a cost-effective low bioink concentration, printing over 3 cm large-scale structures containing human adult stem cells, which were differentiated into chondrocytes. In the present study, peptides IIZK and IIFK were used in combination with RSM to analyze numerous data from rheology measurements to predict stiffness conditions using SPM (Figure S1). The SPM supported the identification of mixture conditions between the two peptides, predicting the formulation of mixed peptide bioinks suitable for 3D bioprinting. Further details on the SPM's modeling and its application to identify specific stiffness regions to formulate peptide-based bioinks are available in the supplementary information (Figures S2–S8, Tables S2–S7). Using the mixed peptide bioinks, it was observed that printing was possible at significantly lower concentrations, using 27.77–37.54% less peptides, compared to when using single peptide bioinks. A mixed

peptide bioink was able to bioprint large-scale trachea-like structures with human-size diameter (Tables 1 & S1). The mixed peptide bioinks were then investigated for bioprinting cell-laden trachea-like constructs that contained either undifferentiated MSCs or chondrocytes differentiated from MSCs. All constructs demonstrated structural stability, elasticity, and self-healing properties. The overall process is schematically shown in Figure 1.

The importance of appropriately selecting the stiffness of the embedding material (bioink/scaffold) for stem cell differentiation—and its effects on cell compatibility, as well as its role in regulating cell development, interaction, and behavior—has been well documented.[74–77] We observed that IIZK showed higher stiffness than IIFK and that the stiffness of the individual bioinks increased with higher peptide concentrations (Figure S9). For the mixed ultrashort peptide bioinks composed of both IIZK and IIFK peptides, a proportional increase of IIZK remarkably enhanced the stiffness of the bioinks (Figures 2 & S8), suggesting that both peptides can simultaneously contribute to bioink stiffness without hindering individual fiber formation. This finding is consistent with prior studies showing that IIZK promotes a more robust fiber assembly than IIFK, primarily due to the characteristic residue cyclohexylalanine (Z).[12]

Due to the interactions between the two peptides, which significantly influence the stiffness of the resulting mixed peptide bioink (Figure S8), under certain mixing conditions, peptide IIFK can behave similarly to IIZK in terms of scaffold stiffness. This can be observed when mixing 2 mg/mL of IIZK with 8 mg/mL of IIFK, resulting in a stiffness of 29.3 kPa, comparable to the 28.4 kPa observed when the ratio was reversed (8 mg/mL IIZK with 2 mg/mL IIFK; Figure S6). In contrast, at lower peptide concentrations, the outcome differed: mixing 5 mg/mL IIZK with 2 mg/mL IIFK resulted in 17.1 kPa, whereas 2 mg/mL IIZK with 5 mg/mL IIFK resulted in 30.8 kPa. Here, the resulting scaffold stiffness is not the same even when containing the same overall amount of material (Figure S6). As shown in Figure 2D**,** a higher proportion of IIFK in the mixture resulted in a stiffness value comparable to pure IIZK. This tunable stiffness behavior aligns with our MD simulation results, where interchangeable peptide effects were observed and attributed to increased intramolecular bonding. Specifically, IIFK formed a higher number of intramolecular bonds during assembly, resembling mixtures with more IIZK (Figure S10). Taken together, these findings highlight that the combination of IIFK and IIZK produces a non-linear effect on the resulting storage modulus. Importantly, IIFK has a stronger influence on scaffold stiffness than IIZK (Figure S8). This emphasizes the importance of understanding the combined effects of different peptides when formulating peptide bioinks and suggests that modeling the interactions between these two peptides requires the consideration of non-linear components (e.g., curvatures by quadratic, polynomial, exponential, and logarithmic relationships).

At higher peptide concentrations, the mixed ultrashort-peptide bioinks showed increased stiffness. However, when IIFK was added to IIZK, the stiffness increase followed a non-linear behavior (Tables S2 & S3). This was supported by statistical analysis using the Pareto chart of standardized effects (Figure S8), demonstrating that the squared term of the model, $IIFK^2$, significantly contributed to the stiffness model, whereas $IIZK^2$ did not (Figure 2D). Therefore, when formulating mixed ultrashort peptide bioinks, it is crucial to consider the interaction between peptides, as they can lead to non-linear relationships.

RSM was used to analyze rheology measurements and develop an SPM for the selection of optimal bioink formulations with specific stiffness suitable for extrusion-based bioprinting of MSCs (Figure 2A). Additional details of the SPM's DOEs and ANOVA results are provided in Tables S4 and S5. To construct the peptide stiffness map for ultrashort peptide scaffolds, 188 rheological measurements were collected. The dataset was then pre-processed to identify outliers. An initial boxplot visualization test revealed six outliers (Figure 2B). Subsequently, the *Z*-score with a threshold of 2.5 and MAD identified one additional outlier (Figure 2C**,** Table S6). Comparison of the boxplot, *Z*-score (Figure 2D**)**, and MAD approaches confirmed the consistent detection of seven outliers, which were removed and replaced with new measurements. The SPM approach, incorporating IIZK and IIFK to model mixed ultrashort-peptide bioinks, is depicted in Figure 2D. Overall, this approach demonstrated high accuracy in predicting the stiffness map based on the proposed RSM equation, as shown by the strong agreement between experimental and predicted measurements (Table S7), and successfully identified several ultrashort peptide bioink formulations with specific stiffness values (Figures 2D & S7).

### 3.2. Identification, formulation, and characterization of mixed ultrashort peptide bioinks

In this study, IIZK and IIFK, differing by an exchange of only one single amino acid Z for F in the peptide sequence, were selected as model peptides for the SPM approach (Figure 3A). In a previous study, these peptides had demonstrated biocompatibility and characteristic stiffness properties, with IIZK being stiffer and IIFK being softer.[12] We assumed that, when using these two peptides to formulate bioink mixtures, it would potentially improve the stiffness tunability, which is important for cell

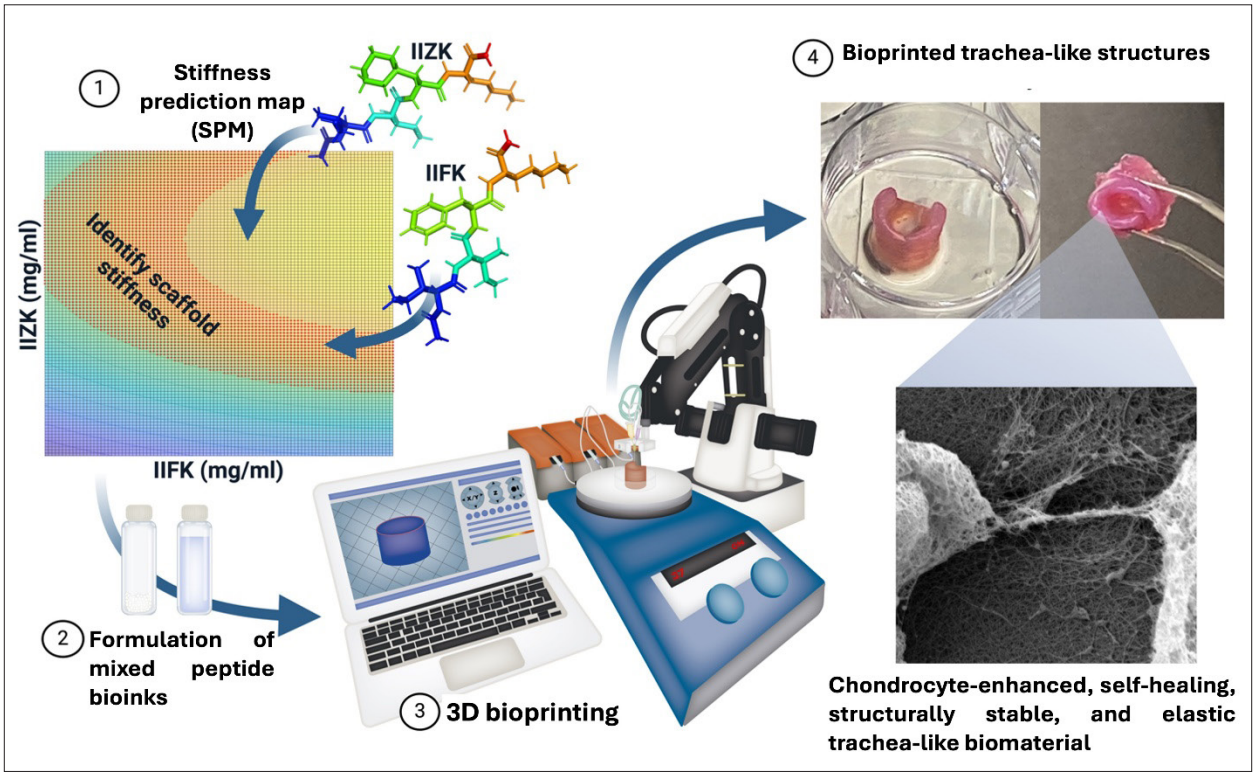


**Figure 1**. Schematic overview of the stiffness prediction map strategy supporting the formulation of optimized mixed ultrashort peptide bioinks for robotic extrusion-based 3D bioprinting of self-healing and elastic trachea-like constructs. Created with BioRender.com.

differentiation. Therefore, the SPM strategy was applied to formulate mixed ultrashort peptide bioinks with tailored stiffness to support chondrogenic differentiation, aiming to enable bioprinting of elastic and structurally stable constructs for tracheal regeneration. The stiffness range was selected based on the scaffold stiffness of the perichondral space, which has been reported as an ideal graft for repairing severe laryngotracheal stenosis due to its high pliability, chondrogenic capacity, mucosalization, and resistance to infection. Additionally, studies have shown that a stiffness of 30 kPa induced the formation of chondrogenic nodules and collagen type II production.[78–80] Therefore, the SPM was used to identify three potential mixed peptide compositions within a stiffness range of 24–34 kPa, closely resembling the chondrocyte stiffness microenvironment (Figure 3B & 3C, Table S13). Using peptides IIZK and IIFK as the underlying scaffold sequences, three mixed ultrashort peptide bioinks were identified and prepared for chondrogenic differentiation.

The SPM correctly predicted the experimental stiffness values of these bioinks to the actual measurements (Table S7), and they were congruent with the theoretical model accuracy (Table S3). Additional factors could further enhance prediction capabilities, such as considering the effects of temperature and pH on the gelation of peptide hydrogels. Stiffness variation in viscoelastic samples can arise due to several reasons, including the material of the rheometer geometries (e.g., stainless steel), instrument inertia, momentum diffusion artifacts, viscoelastic wave propagation (viscous or elastic), surface tension artifacts in rotational geometries, and secondary flows caused by purely elastic instabilities that violate the assumption of homogeneous shear deformation.[81] Therefore, there has been an interest in automated preparation of homogeneous bioinks in 3D bioprinting, which could further improve rheology-based data acquisition of viscoelastic samples.[82]

The selected bioinks exhibited different viscosities and surface tensions (Figure 3D & 3E). These properties have been highlighted as important parameters for the successful 3D bioprinting of bioinks.[83] In this study, the 3:1 IIZK:IIFK mixed peptide bioink exhibited a viscosity similar to that of the 1:3 IIZK:IIFK composition in suspension, suggesting that the 3:1 ratio would be less prone to clogging during extrusion-based bioprinting. Furthermore, both bioinks exhibited surface tensions of approximately 5 mN/m, which reduced bioink adhesion and supported smoother

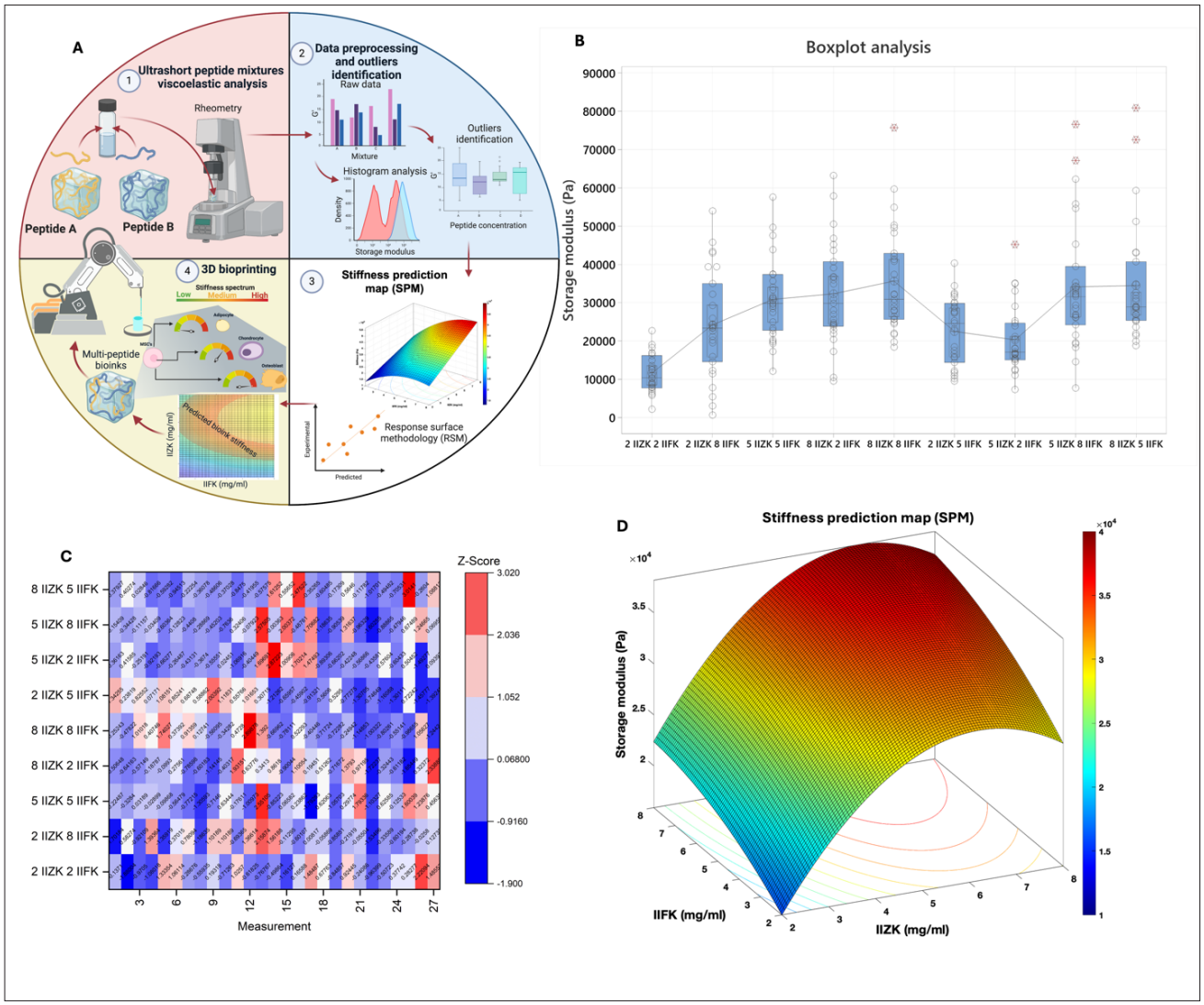


**Figure 2.** Stiffness prediction mapping of peptide bioinks for precise control of the 3D microenvironment stiffness. (A) Schematic representation describing the four steps in the SPM strategy for the development of mixed ultrashort peptide bioinks for extrusion-based 3D bioprinting. (B) Visualization of outliers through boxplot plotting. (C) Identification of outliers according to their *Z*-scores. (D) Stiffness prediction map to identify, predict, and formulate the stiffness of mixed ultrashort peptide bioinks. Figure 2A created with BioRender.com.

extrusion through the microfluidic tubing, ensuring compatibility with the extrusion-based bioprinter. In general, it was observed that bioinks containing higher amounts of IIFK resulted in higher viscosity, while those containing higher amounts of IIZK reduced the viscosity.

The mixed peptide bioinks formed stable fiber assemblies, with the number of intermolecular hydrogen bonds varying according to peptide ratios (Figures 3F & S9–S11, Tables S8–S12). SEM imaging confirmed the formation of fibers in all cases (Figure 3G). Our simulation results suggest that both IIZK and IIFK, when mixed, can form intra- and intermolecular bonds during peptide assembly (Figures S10 & S11). Furthermore, a higher amount of IIFK resulted in hydrogen bond numbers comparable to those of IIZK (Tables S9 & S10), while IIFK formed fewer random coil and more β-turn secondary structures during assembly (Tables S11 & S12). This suggests that IIFK, within mixed ultrashort peptide bioinks, can mimic the assembly behavior of IIZK, enabling high biocompatibility while retaining solid structural properties after bioprinting. This is interesting because IIFK-bioprinted structures have been reported to exhibit lower structural stability and resolution than IIZK-printed structures.[50] Meanwhile,

IIFK is known for excellent cytocompatibility during stem cell proliferation.[12] Therefore, it would be possible to retain both properties in the form of mixed ultrashort-peptide bioinks for extrusion-based bioprinting. Such cooperative assembly is commonly seen in ultrashort-peptide bioinks, where peptides of different properties can assemble into higher-order structures.[47] Moreover, this dual-peptide gelation highlights how molecular pairing tunes the stiffness–softness balance of the resulting bioinks (Tables S9 & S10). AFM topographical analysis of the peptide mixtures revealed a predominant nanofiber diameter of approximately 8.5 nm across all observed fibers (Figure 3H).

AFM topographical analysis of the peptide mixtures revealed different height profiles depending on peptide combinations: 3:1 IIZK:IIFK fibers had an average diameter of 6.54±0.92 nm, 1:1 IIZK:IIFK fibers averaged 7.06±0.49 nm, and 1:3 IIZK:IIFK fibers averaged 7.46±0.45 nm (Figures 3H, S12A–S12C, S13A–S13C, & S14A–S14C). In most cases, the supramolecular handedness of the fibers was not readily discernible, and no consistent helical pitch could be resolved, as can be observed from the sample longitudinal profiles provided in Figures S12D, S12E, S13D, S13E, S14D, and S14E. By contrast, in our previous investigations involving IIZK and IIFK, AFM topography demonstrated distinct helical pitches, with IIFK consistently forming left-handed nanofibers and IIZK forming right-handed ones. In this study, the nanofiber diameters were consistently smaller than those previously reported, which may reflect slower assembly kinetics of the two peptides.

Regarding the fibers of the peptide mixtures, the absence of discrete left-handed and right-handed supramolecular assemblies suggests that the IIZK and IIFK peptides co-assemble along the same nanofiber rather than forming distinct fibers. However, due to the inherent resolution limitations of the AFM technique and convolution effects between the AFM probe and the nanofiber surface, it is currently not possible to unambiguously resolve the precise arrangement of the peptide constituents within individual nanofibers. Additionally, Raman spectral analysis of the Amide I region revealed a predominant sharp peak in the range of 1660 $cm^{-1}$, typical of well-ordered amyloid-like nanofibers with β-turn secondary structure, a kinked structural variant of β-sheets. The slight differences in the values of the Raman peak shift were not significant and can be attributed to the instrument's resolution (Figure 3I). The solubility and gelation properties of the mixed ultrashort-peptide bioinks are provided in Table S13.

TGA was performed on mixed ultrashort peptide and single peptide bioinks to evaluate their composition under thermal changes. In Figure S15**,** a 5% reduction in weight was observed when heating from room temperature to 200°C, attributed to the evaporation of residual solvent and the release of $H_2O$ within the crystalline arrangements, confirming the absence of adsorbed water or solvent molecules across all peptides.[65,84] Subsequently, a further 15% loss was observed when heating from 200 to 250°C in all samples, associated with progressive deamination, decarboxylation, and depolymerization resulting from peptide bond breakage.[85,86] A further 65% loss occurred between 300 and 340°C due to primary decomposition, followed by secondary decomposition from 380 to 650°C, ultimately leading to complete degradation with only residual weight remaining. Additionally, we can observe that the highest rates of decomposition occurred at 230 and 325°C across all samples. The physico-chemical analysis of the peptide mixtures showed that they remained stable up to 332°C (Figure S15). One of the primary advantages of utilizing mixed peptide bioinks lies in their ability to adapt to the desired mechanical stiffness needed for prospective applications. Consequently, in TGA, consistent degradation trends in terms of weight loss versus temperature are discernible for the ultrashort peptides IIZK and IIFK. According to our results (Figure S15), we can conclude that there are no significant changes from a thermomechanical perspective, indicating the stable performance of all mixed bioinks. This stability is crucial for applications where biofabrication is pertinent, allowing for the adjustment of other properties, such as biological and chemical, without interfering with thermal modifications.

### 3.3. 3D bioprinting of trachea-like constructs containing mesenchymal stromal cells

Our robotic 3D bioprinting system has been extensively used with single peptide bioinks to fabricate various cell-laden tissue constructs.[12,15,16,87] As reported earlier, depending on the individual cellular graft of choice, the 3D bioprinting system must be adapted to guarantee a continuous gel deposition by considering the speed of the robotic arm, selecting the suitable nozzle, adjusting the microfluidic pumps, and choosing the correct viscosities of the bioinks. For the bioprinting of trachea-like constructs using mixed peptide bioinks, we adopted a constant flow rate and pulse mode for the automated extrusion of cells, buffer, and peptide solution (Figures 4A & S16, Video S1).

On days 14 and 28, after differentiation of MSCs, no cytotoxicity was observed for the newly generated chondrocytes within the scaffolds (Figure 4G & 4H, see also the cytocompatibility of the non-mixed individual peptide bioinks in Figure S17). The constructs exhibited excellent resolution, formed multiple layers through gel-thread deposition, and showed visibly refined details without

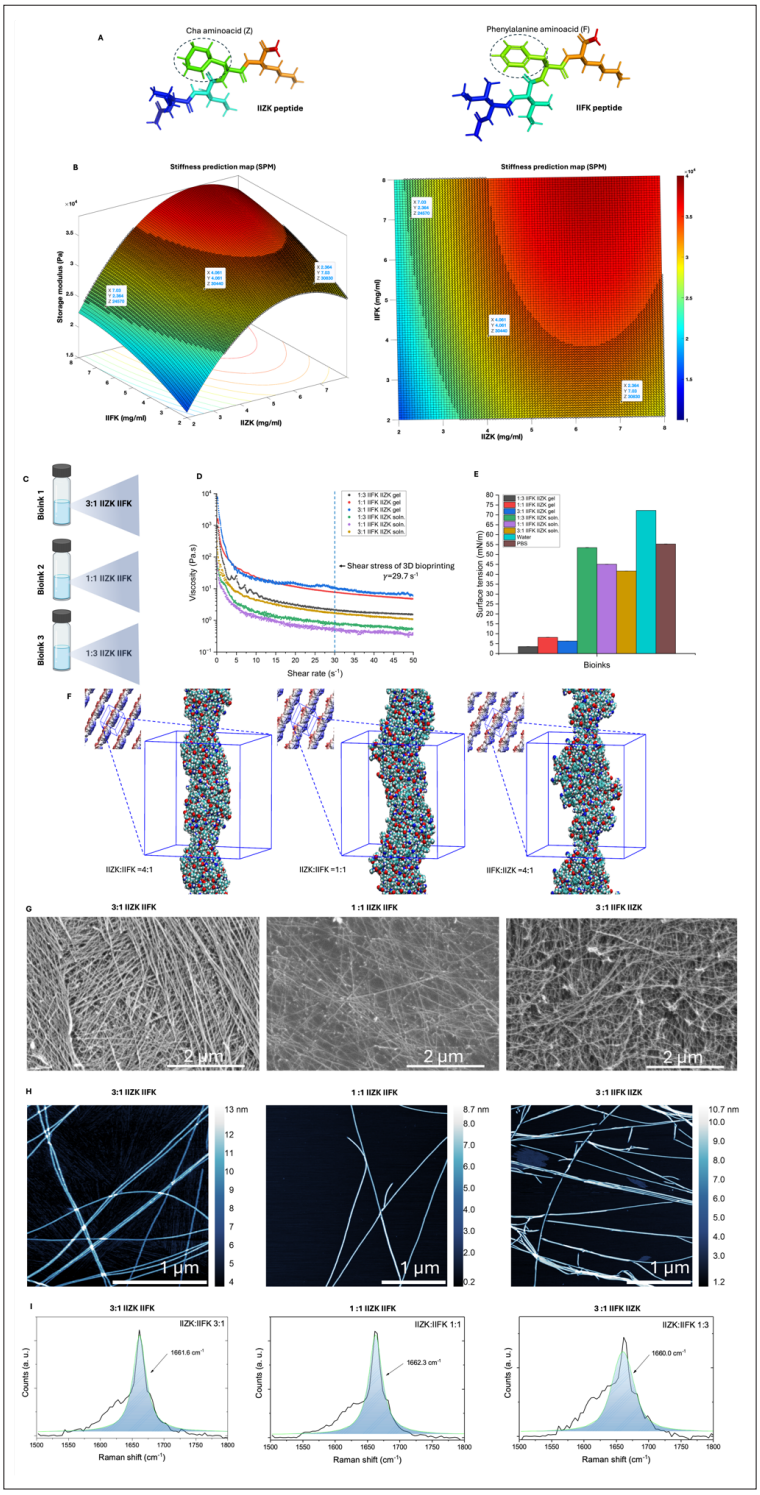


**Figure 3.** Characteristics of IIZK–IIFK peptide mixtures. (A) Structure of peptides IIZK and IIFK. (B) Application of the stiffness prediction map to formulate three bioinks with initial stiffness between 24 and 31 kPa, where the red marks identify the stiffness range. (C) Formulated bioinks and their (D) viscosities and (E) surface tensions. (F) Molecular docking simulations for assembling the mixed ultrashort peptide bioinks for 3D bioprinting. (G) Scanning electron microscopy images (scale bars: 2 µm; magnifications: 25, 000x), (H) atomic force microscopy topography (scale bar: 1 µm; Figure H left, magnification is about 15,000 based on displayed image size of 3x3 cm; Figures H center and right, magnification is about 10,000 based on displayed image size of 3x3 cm), and (I) Raman spectra of the Amide I region of mixed peptide bioink fibers with different ratios: 3:1 IIZK:IIFK (left), 1:1 IIZK:IIFK (center), and 3:1 IIFK:IIZK (right). In Panel I, dark lines indicate the raw data, blue areas/lines represent the central peak in the Amide I region, and the values indicate the prevalent peak value in $cm^{-1}$.

collapsing under their weight or after the addition of media (Figure 4C–4F, Table S1). Among the tested formulations, it was observed that the 3:1 IIZK:IIFK (7.03 and 2.36 mg/mL, respectively) mixed peptide bioink showed the best results for layer deposition and printing resolution, with minimal clogging and clumping during the printing process (Figure 4B & 4C, Video S1). Bioinks with higher IIZK contents exhibited viable, spherical chondrocytes that were better preserved than those from single peptide bioink formulations (Figure S17), while those with higher IIFK contents resulted in lower-resolution constructs (Table S1). Interestingly, a higher proportion of IIZK decreased solubility, whereas IIFK improved it (Table S13), with opposite effects observed for gelation speed. These results are congruent with previous reports showing that IIFK-based bioinks gel more slowly than IIZK-based bioinks at 10 mg/mL.[12] Nonetheless, all mixed formulations were easily printable and formed stable, multilayered structures using 3.60–4.88 mg less peptides than previously reported for bioprinting large-scale constructs.[12,73] This

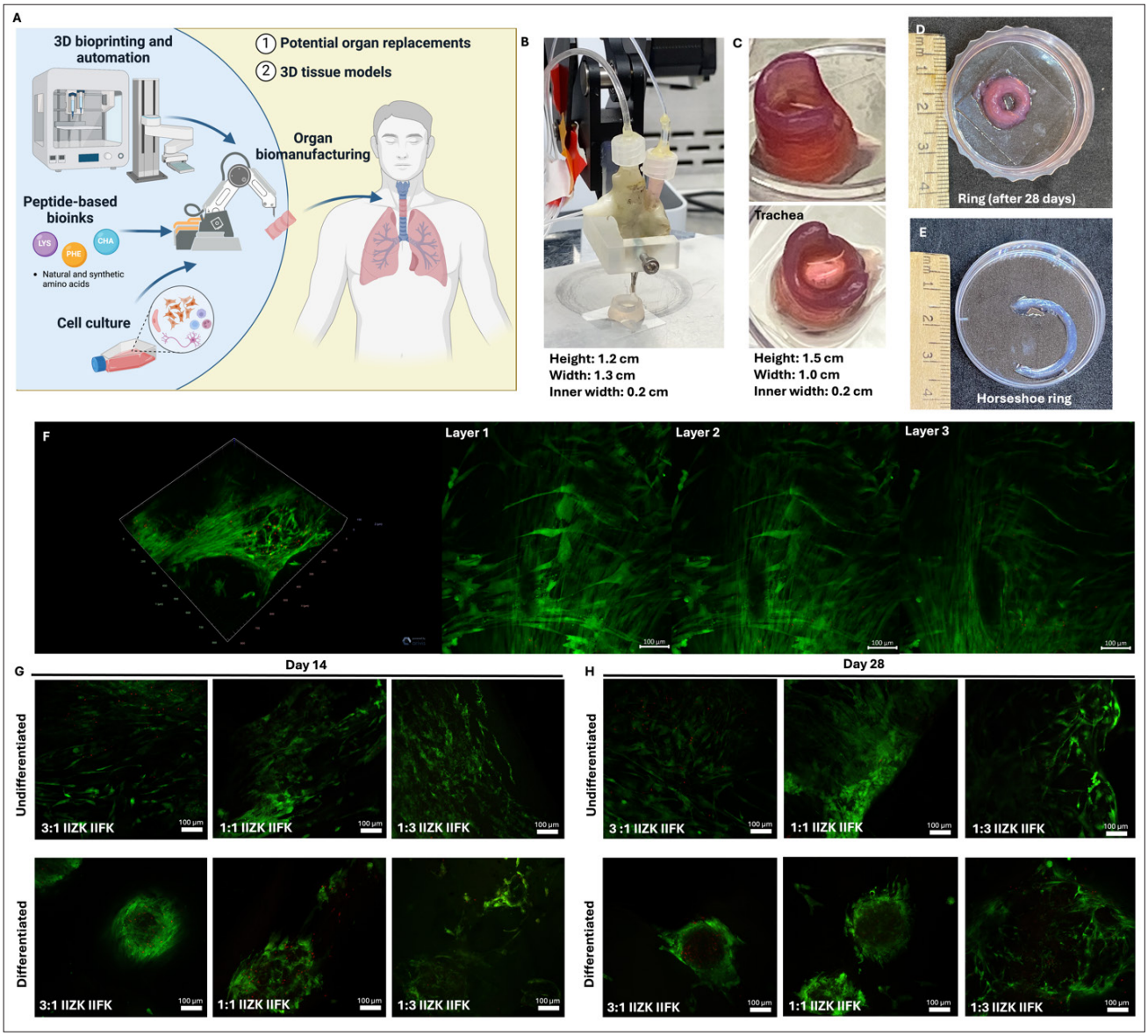


**Figure 4.** Bioink biocompatibility. (A) Schematic overview of the biofabrication procedure generating cell-laden trachea-like structures. (B) Picture of the robotic bioprinter during printing. (C) The trachea-like construct cultures in media. (D) Bioprinted ring structures. (E) "C-shaped" half-cylinder structures. (F) Confocal microscopy images of the bioprinted cell-containing trachea-like constructs after 28 days in culture media (scale bars: 100 µm; magnifications: 20×). Cytocompatibility results of the 3D bioprinted structures at (G) day 14 and (H) day 28 with and without mesenchymal stromal cell differentiation across different IIZK:IIFK ratios (scale bars: 100 µm; magnifications: 20×). Figure 4A created with BioRender.com.

reduction in peptide concentration represents a significant improvement, potentially reducing synthesis costs and promoting overall process sustainability.[88] The viscoelastic properties of these bioinks further underscore their use in the extrusion-based bioprinting of 3D structures (Figure S18). Overall, these findings demonstrate that mixed ultrashort peptide bioinks are highly extrudable, compatible with the robotic 3D bioprinting process, and hold strong potential for upscaling and automated printing of large-scale tissue and organ constructs.

### 3.4. Chondrogenesis and cartilage formation through mesenchymal stromal cell differentiation

Using different mixed peptide bioink formulations, the bioprinted ring structures exhibited distinct morphological features during stem cell differentiation (Figure 5). The presence of dense segments of chondrogenic nodules indicated the presence of several chondrocytes surrounded by a pericellular matrix.[89,90] The formation of chondrogenic nodules was mainly observed in Figures 5A and 5C. This is similar to previous observations where, at higher concentrations, both IIZK and IIFK promote a chondrogenic-like microenvironment. It has been highlighted that stiff to moderately stiff scaffold matrices promote chondrocyte spreading, while softer matrices induce a spherical chondrocyte shape.[91] This is consistent with the observed chondrocyte morphogenesis in this study, where bioinks containing more IIFK exhibited more spheroid chondrocytes (Figure 5A), while those with more IIZK showed dense dark areas due to cell spreading (Figures 5B & 5C).

Gene expression analysis revealed that the 3:1 IIZK:IIFK and the 3:1 IIFK:IIZK (i.e., 1:3 IIZK: IIFK) mixed peptide bioinks showed high expressions of collagen type X, collagen type 2, collagen type 1, *SOX9*, and *RUNX2* (Figure 5G). On the contrary, the *ALPL* gene expression was highest for the 1:1 IIZK:IIFK mixed peptide bioink, with almost no chondrogenic gene expression. The expression of the *SOX5* gene was also observed with the 3:1 IIZK:IIFK mixed peptide bioink. These findings indicate that 1:1 IIZK:IIFK mixed peptide bioink yielded a peptide hydrogel network that was not suitable for chondrogenesis (Figure 3F–3H), potentially due to differences in the amount of differentiated cells, their morphology, and the formation of chondrogenic nodules that successfully condensed into mature cartilage nodules.[92–94] This observation is further supported by the morphogenesis of chondrocytes with this formulation (Figure 5B & 5E). In contrast, the abundance of collagen type II and type X promoted chondrocytes and chondrogenic nodules (Figure 5A–5C), resulting in dense segments distributed throughout the bioprinted trachea-like constructs containing differentiated MSCs.

It has been reported that the expression of collagen type I is found in early chondrocytes, followed by the enrichment of collagen type II for the structural strength of the ECM, and then the essential roles of SOX5 and SOX9 in directing MSC differentiation into chondrocytes for cartilage formation. Lastly, the presence of collagen type X indicates abundant ECM production and hypertrophic chondrocyte formation, highlighting the protein as an essential component for tissue integration and function.[73,95] Furthermore, the viscoelastic properties of the IIZK/IIFK bioinks appeared to further promote chondrogenic nodule formation (Figure S17). Our results parallel previous findings with GelMA-based hydrogels,[96] where chondrocytes showed similar morphology, and gene expression analysis confirmed the production of collagen types I, II, and X (Figure 5G). Specifically, the bioprinted trachea-like constructs printed with 3:1 IIZK:IIFK and 3:1 IIFK:IIZK ratios resulted in higher gene expression of collagen type X, followed by collagen types II and I, consistent with the composition of hyaline cartilage. Collagen type I forms fibers with high tensile strength and is commonly present in articular and meniscal cartilages, as well as bone, dermis, tendon, ligaments, and cornea.[97,98]

Interestingly, previous studies using single IIZK peptide bioinks in 3D bioprinting reported high collagen type II expression but low collagen type I, collagen type X, SOX-9, and aggrecan expressions.[12,73] In contrast, in the present study, the bioink that contained high levels of IIZK induced the expression of all these genes, with particularly high collagen type X expression. The presence of collagen X suggests successful cartilage formation through hypertrophic chondrocytes and serves as a pre-indicator of endochondral ossification.[99,100] It provides strong inter- and intramolecular interactions among network-forming short-chain collagens.[97] It has been found in scaffold-free endotracheal structures transplanted in rabbits, native tracheal cartilage,[98,101,102] deep zone articular cartilage, articular chondrocytes, auricular and nasal cartilages, and during the development of mid-diaphysis. Importantly, its presence does not necessarily imply mineralization.[98] While collagen type X contributes to the structural stability of bioprinted trachea constructs due to its high stiffness properties, it is not sufficient for successful trachea regeneration and may predispose to tracheal stenosis after transplantation.[102] Therefore, the balanced expression of collagens, such as collagen type II, is essential for successful trachea regeneration. This type of biomaterial could also be useful for articular cartilage repair due to its high expression of collagen type X.

### 3.5. Self-healing properties

Next, we analyzed the self-healing properties of the mixed- and individual-peptide bioinks in the presence or absence

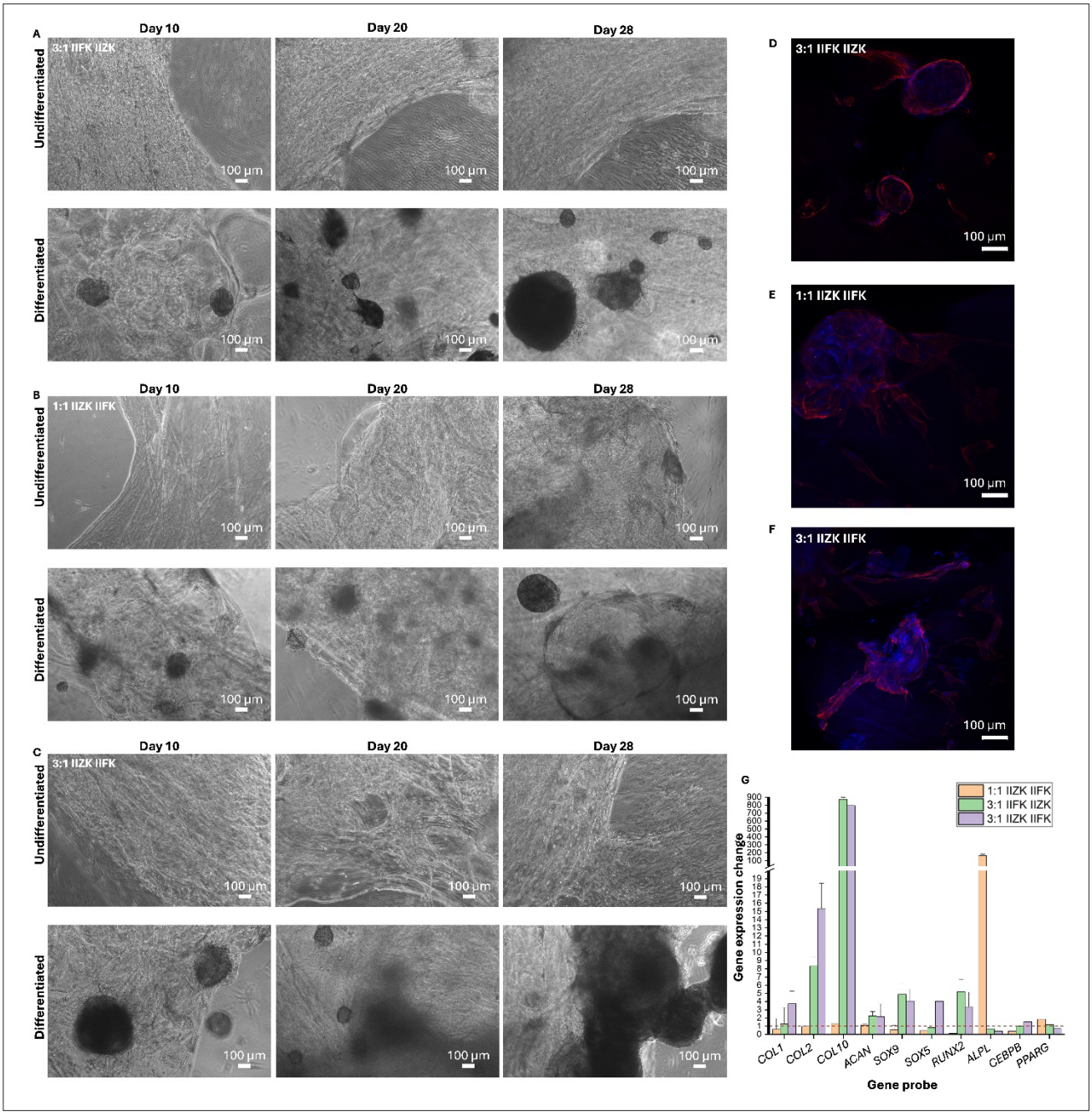


**Figure 5.** Analysis of the differentiation capacity of 3D bioprinted mesenchymal stromal cells (MSCs) using different mixed ultrashort peptide bioink formulations. Undifferentiated and differentiated MSCs embedded in the (A) 3:1 IIFK:IIZK, (B) 1:1 IIZK:IIFK, and (C) 3:1 IIZK:IIFK mixed peptide bioinks (scale bars: 100 µm; magnifications: 40×). (D–F) Fluorescence microscopy images of MSCs showing cytoskeleton staining on day 14 across different peptide ratios using actin-phalloidin and 4',6-diamidino-2-phenylindole (DAPI) (scale bars: 100 µm; magnifications: 20×). (G) Gene expression analysis of differentiated MSCs on day 14 across formulations.

of cells, including undifferentiated MSCs and MSC-derived chondrocytes (Figures 6A, S17, S19, & S20). The circular structures of printed bioinks had full contact with the rheometer probe (Figure 6B–6D). The acellular scaffolds, i.e., bioinks without any cells, exhibited a self-healing capacity between 81.42 and 99.06% (Figure 6N). When the samples were 3D bioprinted with undifferentiated MSCs and incubated for 28 days, their stiffness decreased compared to acellular scaffolds (Figure 6E, 6H, 6K), likely due to cellular reorganization on the 3D scaffolds.

Among the mixed formulations, the self-healing properties of the 3:1 IIZK:IIFK bioink were higher in the presence of chondrocyte-enriched ECM compared to those with undifferentiated MSCs after an incubation of 28 days and a healing time of 60 min (Figure 6N), with a healing efficiency of 94.62%, along with the expression of collagen and the presence of chondrocytes. In comparison, the 3:1 IIFK:IIZK bioink reached 61.65% healing efficiency, while the 1:1 IIZK:IIFK bioink only achieved 29.33%. Conversely, the self-healing capabilities were slower for bioinks containing MSCs, with healing efficiencies between 70.24 and 71.88% (Figure 6F, 6I, 6L, & 6N). Notably, the mixed ultrashort peptide bioinks consistently outperformed individual peptide formulations in terms of self-healing properties (Figures 6N–6P, S19, & S20).

The self-healing properties of our mixed peptide bioinks were found to be faster and more stable than several reported thixotropic polymer-based and nanocomposite hydrogels, such as PDMA hydrogels, telechelic difunctional PEG mixed with glycol chitosan hydrogels, and nanofibrillated cellulose mixed with PVA hydrogels. Overall, the mixed ultrashort peptide bioinks exhibited remarkable self-healing properties comparable to those of PVA functionalized with methyl viologen cellulose nanocrystals, which exhibit near-instantaneous self-recovery.[103] Remarkably, the 3:1 IIZK:IIFK bioink containing chondrocytes demonstrated the most profound and stable self-healing properties in comparison to the other formulations tested in this study.

### 3.6. Changes in viscoelastic behavior during long-term 3D cell culture

Our findings demonstrate that the 3:1 IIZK:IIFK bioink performed remarkably well in terms of printability, cytocompatibility, chondrogenic differentiation, and healing efficiency. These observations, including excellent resolution and structural stability of the bioprinted constructs, support the bioink's superior performance in the bioprinting process of trachea-like structures (Figure 7A & 7B, Table S1). By day 14, confocal microscopy imaging revealed connecting actin filaments within the bioprinted trachea-like structures, with few dead cells (Figure 7C). Furthermore, the presence of undifferentiated MSCs was observed within the bioprinted trachea-like structure, particularly at the sides (Figure 7E). The fibers of the bioprinted scaffold exhibited anisotropic alignment to form the scaffolding 3D structure (Figure 7F). Following 28 days of differentiation, the bioprinted trachea-like structure exhibited the formation of a dense region (Figure 7G) and high elasticity (Figure 7K, Videos S2 & S3), a finding that is consistent with earlier observations. SEM imaging revealed the presence of chondrocytes within this region, accompanied by the formation of filopodia bridges (Figure 7H–7J). An explicit change in the rigidity of the trachea-like structures was evident following a 100-day incubation period (Figure 7L). The bioprinted trachea-like structures, containing MSC-derived chondrocytes, demonstrated a 2.7-fold increase in structural stiffness, while the trachea constructs containing undifferentiated MSCs exhibited a 26.8% decrease in stiffness. The 3D trachea-like constructs were bioprinted in human-size dimensions and then cultured for a period of up to 100 days (Figure 7M–7O, Video S4).

The observed elasticity of the bioprinted trachea-like structures (Figure 7K, Videos S2 & S3) is attributable to the presence of collagen type II, which comprises 90–95% of the collagen in the ECM, especially in hyaline, auricular, epiglottal, nasal, articular, and meniscal cartilages.[98] Collagen type II is a marker of musculoskeletal maturity and comprises, together with glycosaminoglycans, a dominant part of the chondrocytes' microenvironment.[80,104] It forms mixed fibrils with collagen type IX and collagen type XI, promoting tissue elasticity and the formation of hyaline fibrous cartilage. It is also known to form 400-nm-thick crossbanded fibrils with a banding pattern, which constitutes the fibrous cartilage matrix.[97]

The arrangement of collagen fibers in the bioprinted trachea-like structures (Figure 7I & 7J) exhibited a high degree of similarity with previously described cases.[105] The gene expression, the morphology of chondrocytes, and the SEM images all indicated the successful establishment of a collagen type II matrix within the structures. The presence of collagen type II has been shown to reinforce the ECM matrix, thereby enhancing the elasticity of the 3D structures (Figure 7K). However, culturing the trachea-like structures with MSCs for 100 days did not increase biomaterial stiffness. Instead, the storage modulus remained statistically consistent with the initial material stiffness, suggesting that bone marrow-derived MSCs remodeled the scaffold toward a softer tissue. In contrast, when the bioprinted trachea-like structures containing MSC-derived chondrocytes were cultured for a longer period, there was a significant increase in the stiffness of the structure between day 28 and day 100 ($p<0.001$;

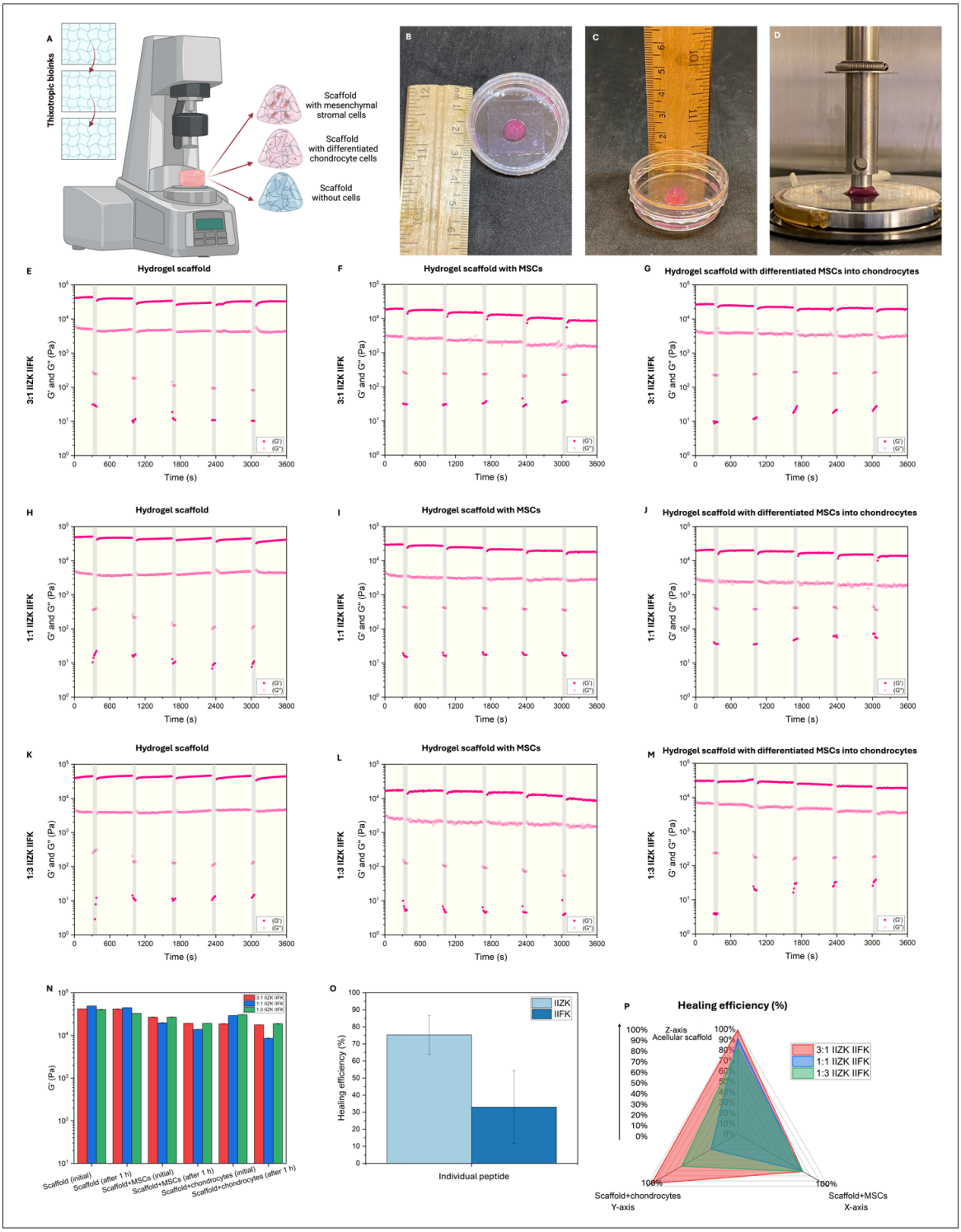


**Figure 6.** Studies on the self-healing capabilities of 3D bioprinted scaffold structures in the presence and absence of mesenchymal stromal cells (MSCs) and MSC-derived chondrocytes on day 28. (A) A schematic representation. (B & C) Images of 3D bioprinted circular structures. (D) Rheological analyses of the viscoelastic behavior of the bioprinted scaffold structures. (E–M) Mixed ultrashort peptide bioinks' self-healing tests (E, H, K) without cells, (F, I, L) in the presence of MSCs, and (G, J, M) in the presence of MSC-derived chondrocytes. (N) Initial and final storage modulus of the bioinks in the presence and absence of undifferentiated MSCs or MSC-derived chondrocytes after inducing self-healing cycles for 1 h. (O & P) Self-healing efficiencies of (O) individual IIZK or IIFK peptide bioinks and (P) mixed ultrashort peptide bioinks. Experiments were performed with alternate step–strain relaxation at 25°C. Figure 6A created with BioRender.com.

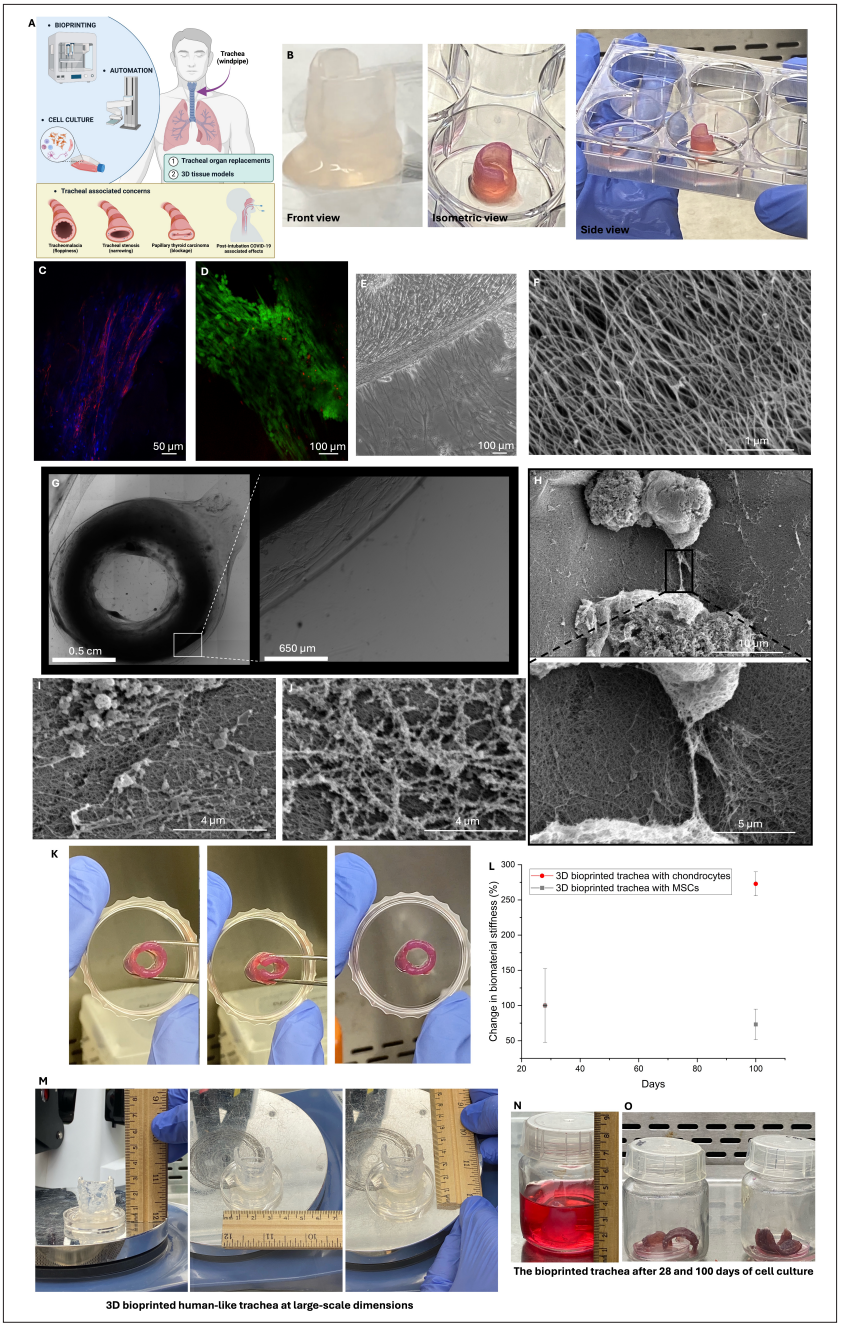


**Figure 7.** 3D bioprinted trachea-like structures fabricated from 3:1 IIZK:IIFK mixed peptide bioinks. (A) An overview of the bioprinting process and the main structural concerns associated with the trachea. (B) A 3D bioprinted trachea-like construct that is 2 cm in height (left), generated through extrusion-based bioprinting. The same construct after 5 days (middle) and 28 days (right) of incubation with cell media. (C) Confocal microscopy of the cytoskeleton (scale bar: 50 µm; magnification: 20×). (D) Live/dead staining of the inner tracheal-like ring (scale bar: 100 µm; magnification: 20×). (E) Phase-contrast microscopy (PCM) image of the outer, tracheal-like ring (scale bar: 100 µm; magnification: 40×). (F) Scanning electron microscopy (SEM) images of the fibers derived from the mixed ultrashort peptide bioink scaffold (scale bar: 1 µm; magnification: 50,000×). (G) PCM images of the bioprinted trachea-like construct on day 28 (scale bar (right): 650 µm; magnification: 20x (right). (H) SEM images show the differentiation of MSCs into chondrocytes and their interaction with the scaffold through filopodia (scale bars: 10 µm [top], 5 µm[bottom]; magnification : 5,000x [top], 12,000 x [bottom]). (I & J) After 28 days, extracellular matrix components were secreted within the fibrous scaffold biomaterial (scale bars: 4 µm; magnifications: 20,000×). (K) Elasticity and structural stability of the bioprinted trachea-like construct on day 28 after stem cell differentiation into chondrocytes. (L) Changes in the biomaterial stiffness after long-term incubation. (M) Extrusion-based 3D bioprinting of a peptide-based human-like tracheal construct with cells at clinically relevant dimensions. (N & O) The biomaterial was subjected to chondrogenic differentiation and cultured for (N) 28 days and (O) up to 100 days. Videos are additionally provided in **Videos S2 & S3**. Figure 7A created with BioRender.com.

Figure 7L). This increase can be attained through the adaptation of the scaffold into a more cartilage-like tissue.

Our findings align with earlier observations on the formation of chondrogenic nodules and their associated gene expression profiles (Figure 5), as well as with the high elasticity exhibited by the bioprinted trachea-like model. This discrepancy in the changes of stiffness may be attributable to the distinct interactions and organization of MSC-derived chondrocytes with the mixed peptide scaffold (Figure 7H) and the ECM components they secrete (Figure 7I & 7J), compared with those secreted by MSCs. These results emphasize the function of cell type in ECM deposition within bioprinted structures. In comparison to undifferentiated MSCs, trachea-like structures containing chondrocytes exhibited a significantly higher storage modulus ($p<0.001$).

The present study employed 3D bioprinting and an SPM to predict scaffold stiffness, with the objective of fabricating trachea-like constructs for healthcare applications. The stiffness map was instrumental in the formulation of three distinct bioinks with pre-tuned stiffness designed to facilitate stromal cell differentiation. These bioinks demonstrated adequate mechanical and physicochemical properties for bioprinting and exhibited compatibility with living tissues, rendering them optimal for chondrogenic nodule formation. The differentiation of MSCs into chondrocytes was facilitated by each bioink, as evidenced by both morphological observations and gene expression analysis (Figure 5). Notably, two bioinks successfully induced the production of collagen type II and type X.

The 3D bioprinted trachea-like constructs exhibited structural stability, elasticity, and self-healing properties, as well as enhanced viscoelastic properties through the deposition of ECM components, visualized through SEM. In addition, the presence of collagen was shown through gene expression analysis. In the future, histochemical analysis of the printed structures could visually facilitate the localization of deposited collagens and glycosaminoglycans. Our findings suggest a new strategy for the bioprinting of tracheal-like structures for trachea regeneration.

## 4. Conclusion

The trachea can face various issues, such as structural deformities, blockages, and other health conditions arising from intubation (e.g., due to SARS-CoV-2 post-intubation effects), as well as aging-related degeneration. Advanced biomaterial is needed for trachea engineering to address these serious issues. Our research focuses on developing 3D bioprinted, elastic, self-healing trachea-like models using mixed ultrashort peptide bioinks. This involves using the RSM to develop an SPM to formulate mixed ultrashort peptide bioinks that enhance MSC differentiation into chondrocytes through the bioink scaffold stiffness architectures. To our knowledge, this is the first report of utilizing the SPM strategy with robotic-assisted extrusion-based 3D bioprinting for developing trachea-like models. The resulting bioinks demonstrated excellent printing resolution, mechanical solid properties, and biocompatibility, promoting hyaline and hypertrophic cartilage formation while exhibiting superior self-healing properties compared to single peptide bioinks. Furthermore, our bioinks also promoted the expression of collagen type X, suggesting potential utility in bone formation studies. After being cultured for up to 100 days, the trachea-like structures further enhanced their mechanical properties, making them suitable for trachea regeneration. This research advances the engineering of trachea-like structures using mixed ultrashort peptide bioinks to develop tracheal models. Future work should include the evaluation of the long-term changes in viscoelasticity through rheology measurements (e.g., evaluation of mixed bioinks' dynamic fiber formation), protein-level validation through Western blotting of key chondrogenic markers (e.g., collagen type II alpha-1, SOX9, and runt-related transcription factor 2), and histochemical staining (e.g., Alcian blue and Safranin O) to complement our current gene expression and morphological evidence. Additional studies will explore AI-driven modeling for the formulation of multi-peptide (≥3) bioinks and integrate epithelial cells into the trachea-like models to investigate the formation of tracheal mucosa. Finally, *in vivo* studies in rabbits or other animal models will be essential to assess the functionality and potential immunogenicity of the trachea-like constructs.

## Acknowledgments

We thank the KAUST Core Labs for their support. We thank Prof. Gabriel Wittum, KAUST, for his feedback on statistical and mathematical modeling. We thank Prof. Abdalla Awidi from The University of Jordan/Cell Therapy Center, Amman, Jordan, for his kind gift of human bone marrow-derived MSCs. We thank the bioprinting group members, particularly Ms. Kowther Kahin and Ms. Zainab Khan, for the development of the robotic 3D bioprinting system, including the dual-coaxial nozzle. We thank Mauricio Aguilar Aguila Isaias for his help with the schematic representation of the 3D robotic arm bioprinter (**Figure 1**). We thank Montserrat del Socorro Valle Perez for the design of the graphical abstract.

## Funding

This research was funded by King Abdullah University of Science and Technology (KAUST) to Charlotte A. E.

Hauser (grant number: Faculty (CH) baseline funding) and Graz University of Technology (TU Graz) for additional funding.

## Conflict of interest

Charlotte A. E. Hauser serves as the Editorial Board Member of the journal, but did not in any way involve in the editorial and peer-review process conducted for this paper, directly or indirectly. Other authors declare they have no competing interests.

## Author contributions

*Conceptualization:* Charlotte A. E. Hauser
*Formal analysis:* Alexander U. Valle-Pérez
*Investigation:* Alexander U. Valle-Pérez, Dana Alhattab, Rui Ge, Eter Othman, Panayiotis Bilalis, Abdulelah Alrashoudi, Antonio Cárdenas-Calvario, Alan Eduardo Avila Ramírez, Zainab N. Khan, Manola Moretti
*Methodology:* Alexander U. Valle-Pérez, Panayiotis Bilalis, Zainab N. Khan, Dana Alhattab, Manola Moretti
*Writing–original draft:* Alexander U. Valle-Pérez, Dana Alhattab, Rui Ge, Manola Moretti
*Writing–review & editing:* Charlotte A.E. Hauser, Christian Baumgartner

## Ethics approval and consent to participate

Not applicable.

## Consent for publication

Not applicable.

## Availability of data

Data is available from the corresponding author upon reasonable request.

## References

1. Murphy SV, Atala A. 3D bioprinting of tissues and organs. *Nat Biotechnol*. 2014;32(8):773-785. doi: 10.1038/nbt.2958
2. Gaharwar AK, Singh I, Khademhosseini A. Engineered biomaterials for in situ tissue regeneration. *Nat Rev Mater*. 2020;5(9):686-705. doi: 10.1038/s41578-020-0209-x
3. Kang HW, Lee SJ, Ko IK, Kengla C, Yoo JJ, Atala A. A 3D bioprinting system to produce human-scale tissue constructs with structural integrity. *Nat Biotechnol*. 2016;34(3): 312-319. doi: 10.1038/nbt.3413
4. Melchels FPW, Domingos MAN, Klein TJ, Malda J, Bartolo PJ, Hutmacher DW. Additive manufacturing of tissues and organs. *Prog Polym Sci*. 2012;37(8):1079-1104. doi: 10.1016/j.progpolymsci.2011.11.007
5. Jorgensen AM, Yoo JJ, Atala A. Solid organ bioprinting: strategies to achieve organ function. *Chem Rev*. 2020;120(19):11093-11127. doi: 10.1021/acs.chemrev.0c00145
6. Low LA, Mummery C, Berridge BR, Austin CP, Tagle DA. Organs-on-chips: into the next decade. *Nat Rev Drug Discov*. 2021;20(5):345-361. doi: 10.1038/s41573-020-0079-3
7. Ingber DE. Human organs-on-chips for disease modelling, drug development and personalized medicine. *Nat Rev Genet*. 2022;23(8):467-491. doi: 10.1038/s41576-022-00466-9
8. Dey M, Ozbolat IT. 3D bioprinting of cells, tissues and organs. *Sci Rep*. 2020;10(1):14023, s41598-020-70086-y. doi: 10.1038/s41598-020-70086-y
9. Shin J, Lee Y, Li Z, Hu J, Park SS, Kim K. Optimized 3D bioprinting technology based on machine learning: A review of recent trends and advances. *Micromachines*. 2022;13(3):363. doi: 10.3390/mi13030363
10. Vanaei S, Parizi MS, Vanaei S, Salemizadehparizi F, Vanaei HR. An overview on materials and techniques in 3D bioprinting toward biomedical application. *Eng Regen*. 2021;2:1-18. doi: 10.1016/j.engreg.2020.12.001
11. Wang Y, Wang J, Ji Z, *et al*. Application of bioprinting in ophthalmology. *Int J Bioprint*. 2022;8(2):552. doi: 10.18063/ijb.v8i2.552
12. Susapto HH, Alhattab D, Abdelrahman S, *et al*. Ultrashort peptide bioinks support automated printing of large-scale constructs assuring long-term survival of printed tissue constructs. *Nano Lett*. 2021;21(7):2719-2729. doi: 10.1021/acs.nanolett.0c04426
13. Huo Y, Xu Y, Wu X, *et al*. Functional trachea reconstruction using 3D-bioprinted native-like tissue architecture based on designable tissue-specific bioinks. *Adv Sci*. 2022;9(29):2202181. doi: 10.1002/advs.202202181
14. Murphy SV, De Coppi P, Atala A. Opportunities and challenges of translational 3D bioprinting. *Nat Biomed Eng*. 2019;4(4):370-380. doi: 10.1038/s41551-019-0471-7
15. Abdelrahman S, Alsanie WF, Khan ZN, *et al*. A Parkinson's disease model composed of 3D bioprinted dopaminergic neurons within a biomimetic peptide scaffold. *Biofabrication*. 2022;14(4):044103. doi: 10.1088/1758-5090/ac7eec
16. Khan ZN, Albalawi HI, Valle-Pérez AU, *et al*. From 3D printed molds to bioprinted scaffolds: A hybrid material

extrusion and vat polymerization bioprinting approach for soft matter constructs. *Mater Sci Addit Manuf*. 2022;1(1):7. doi: 10.18063/msam.v1i1.7

17. Mirdamadi E, Tashman JW, Shiwarski DJ, Palchesko RN, Feinberg AW. Fresh 3D bioprinting a full-size model of the human heart. *ACS Biomater Sci Eng*. 2020;6(11):6453-6459. doi: 10.1021/acsbiomaterials.0c01133

18. Jiang X, Zuo X, Wang H, Zhu P, Kang YJ. Fabrication of vascular grafts using poly(ε-caprolactone) and collagen-encapsuled ADSCs for interposition implantation of abdominal aorta in rhesus monkeys. *ACS Biomater Sci Eng*. 2024;10(5):3120-3135. doi: 10.1021/acsbiomaterials.3c01209

19. He C, Yan J, Fu Y, Guo J, Shi Y, Guo J. Organoid bioprinting strategy and application in biomedicine: a review. *IJB*. 2023;9(6):0112. doi: 10.36922/ijb.0112

20. Hammad NS, Khan ZN, Valle-Pérez AU, Hauser C. A predictive machine learning model to optimize flow rates on an integrated microfluidic pumping system for peptide-based 3D bioprinting. In: Gray BL, Rapp BE, eds. *Microfluidics, BioMEMS, and Medical Microsystems XXI*. SPIE; 2023:3. doi: 10.1117/12.2650440

21. Tang M, Jiang S, Huang X, *et al*. Integration of 3D bioprinting and multi-algorithm machine learning identified glioma susceptibilities and microenvironment characteristics. *Cell Discov*. 2024;10(1):39. doi: 10.1038/s41421-024-00650-7

22. Freeman S, Calabro S, Williams R, Jin S, Ye K. Bioink formulation and machine learning-empowered bioprinting optimization. *Front Bioeng Biotechnol*. 2022;10:913579. doi: 10.3389/fbioe.2022.913579

23. Tebon PJ, Wang B, Markowitz AL, *et al*. Drug screening at single-organoid resolution via bioprinting and interferometry. *Nat Commun*. 2023;14(1):3168. doi: 10.1038/s41467-023-38832-8

24. Trucco D, Sharma A, Manferdini C, *et al*. Modeling and fabrication of silk fibroin–gelatin-based constructs using extrusion-based three-dimensional bioprinting. *ACS Biomater Sci Eng*. 2021;7(7):3306-3320. doi: 10.1021/acsbiomaterials.1c00410

25. Perin F, Spessot E, Famà A, *et al*. Modeling a dynamic printability window on polysaccharide blend inks for extrusion bioprinting. *ACS Biomater Sci Eng*. 2023;9(3):1320-1331. doi: 10.1021/acsbiomaterials.2c01143

26. Zanderigo G, Bracco F, Semeraro Q, Colosimo BM. In-situ printability maps (IPM): a new approach for in-situ printability assessment with application to extrusion-based bioprinting. *Bioprinting*. 2023;36:e00320. doi: 10.1016/j.bprint.2023.e00320

27. Harris CG, Semprini L, Rochefort WE, Fogg KC. Statistical optimization of cell–hydrogel interactions for green microbiology – a tutorial review. *RSC Sustain*. 2024;2(12):3750-3768. doi: 10.1039/D4SU00400K

28. Chung JHY, Naficy S, Yue Z, *et al*. Bio-ink properties and printability for extrusion printing living cells. *Biomater Sci*. 2013;1(7):763. doi: 10.1039/c3bm00012e

29. Hölzl K, Lin S, Tytgat L, Van Vlierberghe S, Gu L, Ovsianikov A. Bioink properties before, during and after 3D bioprinting. *Biofabrication*. 2016;8(3):032002. doi: 10.1088/1758-5090/8/3/032002

30. Khoeini R, Nosrati H, Akbarzadeh A, *et al*. Natural and synthetic bioinks for 3D bioprinting. *Adv NanoBiomed Res*. 2021;1(8):2000097. doi: 10.1002/anbr.202000097

31. Kumar S, Tharayil A, Thomas S. 3D bioprinting of nature-inspired hydrogel inks based on synthetic polymers. *ACS Appl Polym Mater*. 2021;3(8):3685-3701. doi: 10.1021/acsapm.1c00567

32. Cui X, Li J, Hartanto Y, *et al*. Advances in extrusion 3d bioprinting: a focus on multicomponent hydrogel-based bioinks. *Adv Healthc Mater*. 2020;9(15):1901648. doi: 10.1002/adhm.201901648

33. Ashammakhi N, Ahadian S, Xu C, *et al*. Bioinks and bioprinting technologies to make heterogeneous and biomimetic tissue constructs. *Mater Today Bio*. 2019;1:100008. doi: 10.1016/j.mtbio.2019.100008

34. Pérez-Pedroza R, Ávila-Ramírez A, Khan Z, Moretti M, Hauser CAE. Supramolecular biopolymers for tissue engineering. *Adv Polym Technol*. 2021;2021:1-23. doi: 10.1155/2021/8815006

35. Mishra A, Loo Y, Deng R, *et al*. Ultrasmall natural peptides self-assemble to strong temperature-resistant helical fibers in scaffolds suitable for tissue engineering. *Nano Today*. 2011;6(3):232-239. doi: 10.1016/j.nantod.2011.05.001

36. Hauser CAE, Deng R, Mishra A, *et al*. Natural tri- to hexapeptides self-assemble in water to amyloid β-type fiber aggregates by unexpected α-helical intermediate structures. *Proc Natl Acad Sci U S A*. 2011;108(4):1361-1366. doi: 10.1073/pnas.1014796108

37. Khan Z, Kahin K, Rauf S, *et al*. Optimization of a 3D bioprinting process using ultrashort peptide bioinks. *IJB*. 2018;5(1):173. doi: 10.18063/ijb.v5i1.173

38. Pantoja Angles A, Valle-Pérez AU, Hauser C, Mahfouz MM. Microbial biocontainment systems for clinical, agricultural, and industrial applications. *Front Bioeng Biotechnol*. 2022;10:830200. doi: 10.3389/fbioe.2022.830200

39. Li Q, Qi G, Liu X, *et al*. Universal peptide hydrogel for scalable physiological formation and bioprinting of 3d

spheroids from human induced pluripotent stem cells. *Adv Funct Mater*. 2021;31(41):2104046.
doi: 10.1002/adfm.202104046

40. Loo Y, Hauser CAE. Bioprinting synthetic self-assembling peptide hydrogels for biomedical applications. *Biomed Mater*. 2015;11(1):014103.
doi: 10.1088/1748-6041/11/1/014103

41. Alhattab DM, Isaioglou I, Alshehri S, *et al*. Fabrication of a three-dimensional bone marrow niche-like acute myeloid leukemia disease model by an automated and controlled process using a robotic multicellular bioprinting system. *Biomater Res*. 2023;27(1):111.
doi: 10.1186/s40824-023-00457-9

42. Bilalis P, Alrashoudi AA, Susapto HH, *et al*. Dipeptide-based photoreactive instant glue for environmental and biomedical applications. *ACS Appl Mater Interfaces*. 2023;15(40):46710-46720.
doi: 10.1021/acsami.3c10726

43. Perez-Pedroza R, Moretti M, Hauser CAE. Fabrication and characterization of colorectal cancer organoids from SW1222 cell line in ultrashort self-assembling peptide matrix. *JoVE*. 2024;(207):66060.
doi: 10.3791/66060

44. Wang Y, Liu X, Ge R, *et al*. Peptide gel electrolytes for stabilized Zn metal anodes. *ACS Nano*. 2024;18(1): 164-177.
doi: 10.1021/acsnano.3c04414

45. Moretti M, Hountondji M, Ge R, *et al*. Selectively positioned catechol moiety supports ultrashort self-assembling peptide hydrogel adhesion for coral restoration. *Langmuir*. 2023;39(49):17903-17920.
doi: 10.1021/acs.langmuir.3c02553

46. Xu J, Pérez-Pedroza R, Moretti M, *et al*. 3D bioprinting of colon organoids in ultrashort self-assembling and decorated peptide matrices. *IJB*. 2024;0(0):3033.
doi: 10.36922/ijb.3033

47. Sarkar B, Nguyen PK, Gao W, Dondapati A, Siddiqui Z, Kumar VA. Angiogenic self-assembling peptide scaffolds for functional tissue regeneration. *Biomacromolecules*. 2018;19(9):3597-3611.
doi: 10.1021/acs.biomac.8b01137

48. Ng WL, Chua CK, Shen YF. Print me an organ! Why we are not there yet. *Prog Polym Sci*. 2019;97:101145.
doi: 10.1016/j.progpolymsci.2019.101145

49. Tang D. Biofabrication of bone tissue: approaches, challenges and translation for bone regeneration. 2016;83:363-382.
doi: 10.1016/j.biomaterials.2016.01.024

50. de León EHP, Valle-Pérez AU, Khan ZN, Hauser CAE. Intelligent and smart biomaterials for sustainable 3D printing applications. *Curr Opin Biomed Eng*. 2023;26:100450.
doi: 10.1016/j.cobme.2023.100450

51. Crowley C, Birchall M, Seifalian AM. Trachea transplantation: from laboratory to patient: trachea transplantation. *J Tissue Eng Regen Med*. 2015;9(4):357-367.
doi: 10.1002/term.1847

52. Park JH, Ahn M, Park SH, *et al*. 3D bioprinting of a trachea-mimetic cellular construct of a clinically relevant size. *Biomaterials*. 2021;279:121246.
doi: 10.1016/j.biomaterials.2021.121246

53. She Y, Fan Z, Wang L, *et al*. 3D printed biomimetic PCL scaffold as framework interspersed with collagen for long segment tracheal replacement. *Front Cell Dev Biol*. 2021;9:629796.
doi: 10.3389/fcell.2021.629796

54. Xu Y, Guo Y, Li Y, *et al*. Biomimetic trachea regeneration using a modular ring strategy based on poly(sebacoyl diglyceride)/polycaprolactone for segmental trachea defect repair. *Adv Funct Mater*. 2020;30(42):2004276.
doi: 10.1002/adfm.202004276

55. Ke D, Yi H, Est-Witte S, *et al*. Bioprinted trachea constructs with patient-matched design, mechanical and biological properties. *Biofabrication*. 2019;12(1):015022.
doi: 10.1088/1758-5090/ab5354

56. Nomoto M, Nomoto Y, Tada Y, *et al*. Bioengineered trachea using autologous chondrocytes for regeneration of tracheal cartilage in a rabbit model. *Laryngoscope*. 2013;123(9):2195-2201.
doi: 10.1002/lary.23784

57. Tan ZH, Dharmadhikari S, Liu L, *et al*. Regeneration of tracheal neotissue in partially decellularized scaffolds. *NPJ Regen Med*. 2023;8(1):35.
doi: 10.1038/s41536-023-00312-4

58. Weber JF, Rehmani SS, Baig MZ, Jadoon Y, Bhora FY. Successes and failures in tracheal bioengineering: lessons learned. *Ann Thorac Surg*. 2021;112(4):1089-1094.
doi: 10.1016/j.athoracsur.2020.10.021

59. Wei S, Zhang Y, Luo F, Duan K, Li M, Lv G. Tissue-engineered tracheal implants: Advancements, challenges, and clinical considerations. *Bioeng Transl Med*. 2024;9(4):e10671.
doi: 10.1002/btm2.10671

60. Mammana M, Bonis A, Verzeletti V, Dell'Amore A, Rea F. Tracheal tissue engineering: principles and state of the art. *Bioengineering*. 2024;11(2):198.
doi: 10.3390/bioengineering11020198

61. Fux T, Österholm C, Themudo R, Simonson O, Grinnemo KH, Corbascio M. Synthetic tracheal grafts seeded with bone marrow cells fail to generate functional tracheae: first long-term follow-up study. *J Thorac Cardiovasc Surg*. 2020;159(6):2525-2537.e23.
doi: 10.1016/j.jtcvs.2019.09.185

62. Dharmadhikari S, Liu L, Shontz K, *et al*. Deconstructing tissue engineered trachea: assessing the role of synthetic scaffolds, segmental replacement and cell seeding on graft performance. *Acta Biomater*. 2020;102:181-191.

doi: 10.1016/j.actbio.2019.11.008

63. Khan Z, Kahin K, Hauser C. Time-dependent pulsing of microfluidic pumps to enhance 3D bioprinting of peptide bioinks. In: Gray BL, Becker H, eds. *Microfluidics, BioMEMS, and Medical Microsystems XIX*. SPIE; 2021:5. doi: 10.1117/12.2578830

64. Yang J, Rahardja S, Fränti P. Outlier detection: how to threshold outlier scores? In: *Proceedings of the International Conference on Artificial Intelligence, Information Processing and Cloud Computing*. ACM; 2019:1-6. doi: 10.1145/3371425.3371427

65. Avila-Ramírez A, Valle-Perez AU, Susapto HH, *et al*. Ecologically friendly biofunctional ink for reconstruction of rigid living systems under wet conditions. *Int J Bioprint*. 2021;7(4):398. doi: 10.18063/ijb.v7i4.398.

66. Khuri AI, Mukhopadhyay S. Response surface methodology. *WIREs Comput Stat*. 2010;2(2):128-149. doi: 10.1002/wics.73

67. Jorgensen WL, Tirado-Rives J. Potential energy functions for atomic-level simulations of water and organic and biomolecular systems. *Proc Natl Acad Sci U S A*. 2005;102(19):6665-6670. doi: 10.1073/pnas.0408037102

68. Abraham MJ, Murtola T, Schulz R, *et al*. GROMACS: High performance molecular simulations through multi-level parallelism from laptops to supercomputers. *SoftwareX*. 2015;1-2:19-25. doi: 10.1016/j.softx.2015.06.001

69. Dodda LS, Cabeza de Vaca I, Tirado-Rives J, Jorgensen WL. LigParGen web server: an automatic OPLS-AA parameter generator for organic ligands. *Nucleic Acids Res*. 2017;45(W1):W331-W336. doi: 10.1093/nar/gkx312

70. Darden T, York D, Pedersen L. Particle mesh Ewald: An $N \cdot \log(N)$ method for Ewald sums in large systems. *J Chem Phys*. 1993;98(12):10089-10092. doi: 10.1063/1.464397

71. Berendsen HJC, Postma JPM, Van Gunsteren WF, DiNola A, Haak JR. Molecular dynamics with coupling to an external bath. *J Chem Phys*. 1984;81(8):3684-3690. doi: 10.1063/1.448118

72. Bussi G, Donadio D, Parrinello M. Canonical sampling through velocity rescaling. *J Chem Phys*. 2007;126(1):014101. doi: 10.1063/1.2408420

73. Alhattab D, Khan Z, Alshehri S, H. Susapto H, A. E. Hauser C. 3D bioprinting of ultrashort self-assembling peptides to engineer scaffolds with different matrix stiffness for chondrogenesis. *Int J Bioprint*. 2023;9(4):719. doi: 10.18063/ijb.719

74. Chaudhuri O, Cooper-White J, Janmey PA, Mooney DJ, Shenoy VB. Effects of extracellular matrix viscoelasticity on cellular behaviour. *Nature*. 2020;584(7822):535-546. doi: 10.1038/s41586-020-2612-2

75. Chaudhuri O, Koshy ST, Branco Da Cunha C, *et al*. Extracellular matrix stiffness and composition jointly regulate the induction of malignant phenotypes in mammary epithelium. *Nat Mater*. 2014;13(10):970-978. doi: 10.1038/nmat4009

76. Wen JH, Vincent LG, Fuhrmann A, *et al*. Interplay of matrix stiffness and protein tethering in stem cell differentiation. *Nat Mater*. 2014;13(10):979-987. doi: 10.1038/nmat4051

77. Kumar S. Stiffness does matter. *Nat Mater*. 2014;13(10):918-920. doi: 10.1038/nmat4094

78. Foyt DA, Taheem DK, Ferreira SA, *et al*. Hypoxia impacts human MSC response to substrate stiffness during chondrogenic differentiation. *Acta Biomater*. 2019;89:73-83. doi: 10.1016/j.actbio.2019.03.002

79. Hartig G, Esclamado R, Telian S. Comparison of the chondrogenic potential of free and vascularized perichondrium in the airway. *Ann Otol Rhinol Laryngol*. 1994;103(1):9-15. doi: 10.1177/000348949410300102

80. Bachmann B, Spitz S, Schädl B, *et al*. Stiffness matters: fine-tuned hydrogel elasticity alters chondrogenic redifferentiation. *Front Bioeng Biotechnol*. 2020;8:373. doi: 10.3389/fbioe.2020.00373

81. Spagnolie SE, ed. *Complex Fluids in Biological Systems: Experiment, Theory, and Computation*. New York: Springer; 2015. doi: 10.1007/978-1-4939-2065-5

82. Wu D, Pang S, Röhrs V, *et al*. Man vs. machine: automated bioink mixing device improves reliability and reproducibility of bioprinting results compared to human operators. *IJB*. 2024;10(2):1974. doi: 10.36922/ijb.1974

83. Ning L, Gil CJ, Hwang B, *et al*. Biomechanical factors in three-dimensional tissue bioprinting. *Appl Phys Rev*. 2020;7(4):041319. doi: 10.1063/5.0023206

84. Giri RS, Mandal B. Boc-Val-Val-OMe (Aβ39–40) and Boc-Ile-Ala-OMe (Aβ41–42) crystallize in a parallel β-sheet arrangement but generate a different morphology. *CrystEngComm*. 2018;20(31):4441-4448. doi: 10.1039/C8CE00097B

85. Dandurand J, Samouillan V, Lacoste-Ferre MH, Lacabanne C, B.Bochicchio, Pepe A. Conformational and thermal characterization of a synthetic peptidic fragment inspired from human tropoelastin: signature of the amyloid fibers. *Pathol Biol*. 2014;62(2):100-107. doi: 10.1016/j.patbio.2014.02.001

86. Qian Y, Engel MH, Macko SA, Carpenter S, Deming JW. Kinetics of peptide hydrolysis and amino acid decomposition at high temperature. *Geochim Cosmochim Acta*. 1993;57(14):3281-3293.
doi: 10.1016/0016-7037(93)90540-D

87. Kahin K, Khan Z, Albagami M, *et al*. Development of a robotic 3D bioprinting and microfluidic pumping system for tissue and organ engineering. In: Gray BL, Becker H, eds. *Microfluidics, BioMEMS, and Medical Microsystems XVII*. SPIE; 2019:25.
doi: 10.1117/12.2507237

88. Isidro-Llobet A, Kenworthy MN, Mukherjee S, *et al*. Sustainability challenges in peptide synthesis and purification: from R&D to production. *J Org Chem*. 2019;84(8):4615-4628.
doi: 10.1021/acs.joc.8b03001

89. Lotz MK, Otsuki S, Grogan SP, Sah R, Terkeltaub R, D'Lima D. Cartilage cell clusters. *Arthritis Rheum*. 2010;62(8):2206-2218.
doi: 10.1002/art.27528

90. Matta C, Mobasheri A. Regulation of chondrogenesis by protein kinase C: emerging new roles in calcium signalling. *Cell Signal*. 2014;26(5):979-1000.
doi: 10.1016/j.cellsig.2014.01.011

91. Zhang Q, Yu Y, Zhao H. The effect of matrix stiffness on biomechanical properties of chondrocytes. *ABBS*. 2016;48(10):958-965.
doi: 10.1093/abbs/gmw087

92. Malko AV, Villagomez M, Aubin JE, Opas M. Both chondroinduction and proliferation account for growth of cartilage nodules in mouse limb bud cultures. *Stem Cell Rev Rep*. 2013;9(2):121-131.
doi: 10.1007/s12015-013-9434-7

93. Sarem M, Otto O, Tanaka S, Shastri VP. Cell number in mesenchymal stem cell aggregates dictates cell stiffness and chondrogenesis. *Stem Cell Res Ther*. 2019;10(1):10.
doi: 10.1186/s13287-018-1103-y

94. Rolfe RA, Shea CA, Murphy P. Geometric analysis of chondrogenic self-organisation of embryonic limb bud cells in micromass culture. *Cell Tissue Res*. 2022;388(1): 49-62.
doi: 10.1007/s00441-021-03564-y

95. Lefebvre V, Behringer RR, De Crombrugghe B. L-Sox5, Sox6 and Sox9 control essential steps of the chondrocyte differentiation pathway. *Osteoarthritis Cartilage*. 2001;9 Suppl A:S69-S75.
doi: 10.1053/joca.2001.0447

96. De Moor L, Fernandez S, Vercruysse C, *et al*. Hybrid bioprinting of chondrogenically induced human mesenchymal stem cell spheroids. *Front Bioeng Biotechnol*. 2020;8:484.
doi: 10.3389/fbioe.2020.00484

97. Von Der Mark K. Structure, biosynthesis and gene regulation of collagens in cartilage and bone. In: *Dynamics of Bone and Cartilage Metabolism*. Erlangen, Germany: Elsevier; 2006:3-40.
doi: 10.1016/B978-012088562-6/50002-9

98. Naumann A, Dennis JE, Awadallah A, *et al*. Immunochemical and Mechanical Characterization of Cartilage Subtypes in Rabbit. 2002;50(8):1049-1058.
doi: 10.1177/002215540205000807

99. Department of Oral and Maxillofacial Surgery, Special Dental Care and Orthodontics, Erasmus MC, 3000 DR Rotterdam, the Netherlands, Knuth C, Andres Sastre E, *et al*. Collagen type X is essential for successful mesenchymal stem cell-mediated cartilage formation and subsequent endochondral ossification. *eCM*. 2019;38: 106-122.
doi: 10.22203/eCM.v038a09

100. He Y, Siebuhr AS, Brandt-Hansen NU, *et al*. Type X collagen levels are elevated in serum from human osteoarthritis patients and associated with biomarkers of cartilage degradation and inflammation. *BMC Musculoskelet Disord*. 2014;15(1):309.
doi: 10.1186/1471-2474-15-309

101. Sasano Y, Takahashi I, Mizoguchi I, Kagayama M, Takita H, Kuboki Y. Type X collagen is not localized in hypertrophic or calcified cartilage in the developing rat trachea. *Anat Embryol*. 1998;197(5):399-403.
doi: 10.1007/s004290050151

102. Weidenbecher M, Tucker HM, Gilpin DA, Dennis JE. Tissue-engineered trachea for airway reconstruction. *Laryngoscope*. 2009;119(11):2118-2123.
doi: 10.1002/lary.20700

103. Taylor DL, In Het Panhuis M. Self-healing hydrogels. *Adv Mater*. 2016;28(41):9060-9093.
doi: 10.1002/adma.201601613

104. Sophia Fox AJ, Bedi A, Rodeo SA. The basic science of articular cartilage: structure, composition, and function. *Sports Health*. 2009;1(6):461-468.
doi: 10.1177/1941738109350438

105. Villegas DF, Donahue TLH. Collagen morphology in human meniscal attachments: a SEM study. *Connect Tissue Res*. 2010;51(5):327-336.
doi: 10.3109/03008200903349639